



# Linking elastic properties of various carbonate rocks to their microstructure by coupling nanoindentation and SEM-EDS

Yousseuf Abdallah, Matthieu Vandamme, Camille Chateau, Denis Garnier, Isabelle Jolivet, Atef Onaisi, Dimitri Richard, Soroosh Zandi

## ► To cite this version:

Yousseuf Abdallah, Matthieu Vandamme, Camille Chateau, Denis Garnier, Isabelle Jolivet, et al.. Linking elastic properties of various carbonate rocks to their microstructure by coupling nanoindentation and SEM-EDS. International Journal of Rock Mechanics and Mining Sciences, 2023, 170, pp.105456. 10.1016/j.ijrmms.2023.105456 . hal-04165900

**HAL Id: hal-04165900**

**<https://enpc.hal.science/hal-04165900>**

Submitted on 19 Jul 2023

**HAL** is a multi-disciplinary open access archive for the deposit and dissemination of scientific research documents, whether they are published or not. The documents may come from teaching and research institutions in France or abroad, or from public or private research centers.

L'archive ouverte pluridisciplinaire **HAL**, est destinée au dépôt et à la diffusion de documents scientifiques de niveau recherche, publiés ou non, émanant des établissements d'enseignement et de recherche français ou étrangers, des laboratoires publics ou privés.

# Linking Elastic Properties of Various Carbonate Rocks to their Microstructure by Coupling Nanoindentation and SEM-EDS

Youssef Abdallah<sup>a,1</sup>, Matthieu Vandamme<sup>a</sup>, Camille Chateau<sup>a,\*</sup>, Denis Garnier<sup>a</sup>,  
Isabelle Jolivet<sup>b,2</sup>, Atef Onaisi<sup>b</sup>, Dimitri Richard<sup>b,3</sup> and Soroosh Zandi<sup>c</sup>

<sup>a</sup>Navier, Ecole des Ponts, Univ Gustave Eiffel, CNRS, Marne-la-Vallée, France

<sup>b</sup>Total, CSTJF, Pau, France

<sup>c</sup>CS GROUP, Pau, France

## ARTICLE INFO

### Keywords:


Carbonate Rocks  
Elastic Properties  
Nanoindentation  
SEM-EDS Analyses  
Homogenization.

## ABSTRACT

Characterizing the elastic properties of carbonate rocks is a crucial parameter in geotechnical and reservoir engineering. However, these natural materials exhibit a wide variety of microstructures, even when they belong to the same facies, leading to a significant dispersion of their elastic properties. We focus on six selected rocks, for which global porosity is shown to be not the only factor controlling elasticity. This study aims to understand which additional microstructural parameters impact the rocks' elastic properties by means of nanoindentation coupled with microscopic observations and analyses. A complete procedure is developed to combine nanoindentation measurements with Scanning Electron Microscopy (SEM) - Energy Dispersive Spectroscopy (EDS) analyses to identify volume fractions and elastic properties of the mineral phases in each rock. The macroscopic Young's moduli are estimated using analytical homogenization and are finally compared with the values obtained from macroscopic experiments. We find that the mineral composition and mechanical properties are critical parameters involved in carbonate rocks' elastic behavior. However, while capturing the overall trend, homogenization is found to overestimate Young's modulus. A discussion on the possible impact of cracks and non-spherical pores is conducted to explain this overestimation. Besides, microindentation tests are carried out to explore higher scales, which remain too small, however, to characterize the macroscopic Young's modulus of carbonate rocks.

**NOTICE:** This is a post-peer-review, pre-copyedit version of an article published in *International Journal of Rock Mechanics & Mining Sciences* 170 (2023). The final authenticated version is available online at: <https://doi.org/10.1016/j.ijrmms.2023.105456>.

\*Corresponding author

 [camille.chateau@enpc.fr](mailto:camille.chateau@enpc.fr) (C. Chateau)

ORCID(s):

<sup>1</sup>Present address : Terrasol, Paris, France

<sup>2</sup>Present address : TotalEnergies, CSTJF, Pau, France

<sup>3</sup>Present address : CVA engineering, Pau, France

## 36 List of Symbols

$E_{exp}$	Macroscopic Young's modulus measured through mechanical tests
$E_{ref}$	Reference value for the Young's modulus
$E_{MT}^{hom}$	Homogenized Young's modulus using Mori-Tanaka schemes
$E_{SC}^{hom}$	Homogenized Young's modulus using self-consistent schemes
$E_{hom}^h$	Homogenized Young's modulus calculated with a consideration of cracks in the dominant phase
$E_{hom}^\alpha$	Homogenized Young's modulus calculated with a consideration of spheroidal shape of pores
$E$	Young's modulus
$K$	Bulk modulus
$G$	Shear modulus
$\nu$	Poisson's ratio
$n$	Number of phases in the material
$h$	Penetration depth of the indenter
$F$	Force applied with the indenter
$L$	Linear dimension of the probed volume by indentation
$M$	Indentation modulus
$H$	Indentation hardness
$S$	Unloading stiffness
$A_c$	Projected contact area
$R_a$	Arithmetic roughness
$R_q$	Quadratic roughness
$f_i$	Volume fraction of the phase $i$
$d$	Distance of an imprint to the nearest interface
$d_{th}$	Threshold on the distance $d$
$\phi$	Porosity volume fraction
$\phi_{macro}$	Macroporosity volume fraction
$\phi_{micro}$	Microporosity volume fraction
$\mu_X$	Mean value of the quantity $X$
$\sigma_X$	Standard deviation of the quantity $X$
$t$	Thickness of an elliptic crack
$w$	Width of an elliptic crack
$l$	Length of an elliptic crack
$\eta$	Crack density parameter
$N$	Number of cracks per unit volume
$A$	Area of an elliptic crack
$P$	Perimeter of an elliptic crack
$\alpha$	Aspect ratio of a spheroidal shape

## 38 1. Introduction

39 Sedimentary rocks, formed through diagenetic processes occurring after the deposition of sediments, cover around  
 40 73% of the Earth's land surface<sup>1</sup>, and consequently, constitute potential reservoirs for hydrocarbons, CO<sub>2</sub> storage,  
 41 and geothermal energy<sup>2,3</sup>. Carbonate rocks are amongst the most complex sedimentary rocks, as they exhibit a large  
 42 variety of microstructural features due to the complexity of their diagenesis<sup>4,5</sup>. According to Flügel<sup>6</sup>, carbonate  
 43 rocks hold between 40% and 60% of oil and gas reserves worldwide. Hence, there is a need to characterize the  
 44 mechanical behavior of carbonate rocks in reservoir engineering. In this study, we focus on the elastic behavior of  
 45 carbonate rocks.

46 Several macroscopic experiments performed on samples of carbonate rocks having similar porosities have shown  
 47 a wide dispersion of elastic modulus<sup>5</sup>, proving that the global porosity is not the only factor controlling the elastic  
 48 behavior. Many additional microstructural features, such as the volumetric ratio of grains to matrix, the presence,  
 49 and type of cementation, the pore types, and the mineral composition, may be involved in the dispersion of the

elastic properties<sup>5,7-9</sup>. Consequently, the prediction of macroscopic elastic moduli of carbonate rocks from the knowledge of its microstructure and of the mechanical properties of its various microscopic phases remains a challenging task.

This study investigates the elastic properties of carbonate rocks having comparable porosities through experiments performed at the microscopic scale to understand the dispersion of macroscopic Young's modulus in light of the microstructural attributes. Several rocks, having comparable porosities but different macroscopic Young's moduli, are considered here. Our study is composed of an experimental part followed by a modeling approach based on the homogenization theory. The instrumented nanoindentation technique<sup>10</sup>, which allows characterizing the localized mechanical properties of every single phase of a material at the microscale level, is used here. This technique has been increasingly carried out on rocks in the last decade since macroscale laboratory tests are not sufficient to investigate the impact of microstructure (see the review of Ma et al.<sup>11</sup> and the references therein). However, few studies have been conducted on carbonate rocks with nanoindentation compared to other types of rock. Nanoindentation has been used on carbonates to assess the heterogeneity of the microscopic mechanical properties<sup>12,13</sup> and to characterize the impact of chemical interactions with the pore fluid (i.e., water<sup>14</sup>, brine<sup>15</sup>, CO<sub>2</sub>-saturated brine<sup>15</sup>, or supercritical CO<sub>2</sub><sup>16</sup>) on the matrix microscopic mechanical properties. Nanoindentation measurements on carbonates have been upscaled to predict macroscopic stiffness, by using a self-consistent scheme<sup>12</sup> or a lattice spring model<sup>17</sup>, with the predictions being compared with macroscopic ultrasound measurements. All those nanoindentation studies on carbonates focused on one or two rocks. On geomaterials or cement-based materials, or even on bones<sup>18</sup>, nanoindentation tests can be combined with several techniques to identify the phases of the studied material, such as optical microscopy<sup>19</sup>, Scanning Electron Microscopy (SEM)<sup>18</sup>, Energy Dispersive Spectroscopy (EDS)<sup>20-31</sup>, Wave Dispersion Spectroscopy (WDS)<sup>32</sup>, X-Ray microtomography<sup>33,34</sup>, confocal laser scanning microscopy<sup>35</sup> and other imaging techniques<sup>36</sup>.

Several groups employed a combined use of nanoindentation and SEM-EDS or EDX on shales. Kumar et al.<sup>24</sup> used EDS mapping over the grid indentation and found a correlation between the elemental heterogeneity of the scanned region and the spread in indentation results. Mason et al.<sup>25</sup> performed grids of indentation on Marcellus shales with various lithofacies. They then observed each indent with SEM and SEM-EDS and determined mineralogy at the location of the indent. They studied how the properties of the individual phases depend on the lithofacies. Abedi et al.<sup>21</sup> employed the combined use of nanoindentation and SEM-EDS to identify what indents were performed on pure phases, mixtures, and close to interfaces, such that they could measure the properties of the fundamental building blocks of the material; they found out that stiffness and hardness of clay/kerogen-rich phases exhibit a unique scaling relation. Mashhadian et al.<sup>22</sup> employed a combination of the two techniques to obtain phase properties that they input into micromechanical models; they found results from the upscaling in good agreement with macroscopic measurements. Veytskin et al.<sup>23</sup> coupled nanoindentation with both SEM-EDS and SEM-WDS to study shales; they showed that the nano-mechanical properties and morphologies of the various phases are distinct. More recently, Liu et al.<sup>20</sup> combined nanoindentation with SEM-EDS and XRD techniques to obtain the mechanical properties of individual phases in four shales; they showed in particular that the properties of these individual phases at the nanoscale are quite diverse.

For what concerns cement-based materials, one can also find several studies that combined nanoindentation with SEM-EDS or EDX. From a combined application of nanoindentation and SEM-EDS to low water-to-cement ratio cement pastes, Chen et al.<sup>26</sup> found evidence for the formation of nanocomposites of calcium silicate hydrates (C-S-H) with nanoportlandite. Moser et al.<sup>28</sup> combined nanoindentation with SEM-EDS mapping to identify indents performed on hydrates in ultra-high-performance concrete. Wilson et al.<sup>27</sup> also combined statistical nanoindentation and SEM-EDS of cement pastes with large replacements of cement by natural pozzolan; they showed that the replacement by natural pozzolan leads to a transformation of C-S-H into C-A-S-H (calcium aluminates silicate hydrates) and to the consumption of portlandite. Sorelli et al.<sup>30</sup> combined nanoindentation and SEM-EDS on cement paste to identify indents performed in pure phases and hence avoid the need for deconvolution. Bu et al.<sup>31</sup> used SEM-EDS to obtain the composition at the location of individual indents in cement paste; they showed that portlandite increases both the indentation modulus and the contact creep modulus. Zhang et al.<sup>29</sup> characterized slag rims in cement-slag systems by a combined use of nanoindentation and SEM-EDS.

In contrast, on carbonates, correlation of nanoindentation results with the local microstructure was performed based on optical microscopy or SEM imaging and, for one limestone lithofacies in a Marcellus shale only, based on SEM-EDS<sup>25</sup>.



In the present study, the nanoindentation technique is coupled with Scanning Electron Microscopy (SEM) and Energy Dispersive Spectroscopy (EDS) to characterize the microstructure of the rocks and identify the mineralogy under the indentation sites. Once the indentation grids are carried out on a sample, SEM-EDS analyses are performed in ex-situ conditions. A method to identify the imprints, whose size is small, in the microscope, has been developed and is presented here. Each indentation test can be consequently attributed to the corresponding phase, and the elastic properties of each phase are obtained. Besides, an EDS map is performed on each sample's whole surface to evaluate the solid phases' volume fractions. In addition, Mercury Intrusion Porosimetry (MIP) tests are carried out to assess the pore size distribution and evaluate the volume fractions of the porosity families. Based on these observations, a simple multiscale scheme of the microstructure is proposed for each rock. Then, analytical homogenization models are used to estimate the rocks' macroscopic Young's moduli from the heterogeneous local moduli, the assessed volume fractions of the different phases constituting the rock, and the proposed microstructural scheme. Finally, the estimated values of the macroscopic Young's modulus are compared to the measured ones from macroscopic experiments.

To the light of the literature presented in the previous paragraphs, our study presents several aspects that are original for carbonates: 1) use of SEM-EDS mapping in complement to nanoindentation testing to identify the mineralogy at the indent location, 2) extensive use and discussion of micromechanical modeling to predict macroscopic stiffness, 3) experimental study of a relatively large number of rocks (i.e., six rocks) of various facieses and mineralogical compositions. 4) Also, our methodological developments regarding the combined use of nanoindentation grids with SEM-EDS mapping make it possible to automatize the characterization of the mineralogical composition at each indent location. 5) The adopted procedure will also serve to conduct a critical analysis of the simple use of the deconvolution technique, usually applied when no imaging is performed<sup>37</sup>. In fact, the deconvolution technique is known to lack robustness, in particular on cement-based materials, in the sense that the mechanical properties deconvoluted for each phase may depend on how the deconvolution procedure is performed<sup>38</sup>. In our present work, we aim at providing a critical analysis of the deconvolution procedure, but for carbonate rocks. Finally, note that the Python codes relative to the current study are available for interested readers in the link given at the end of this paper.

The current paper is organized into six sections, besides this introductory section. In Section 2, the material is presented, as well as the experimental procedure. Then, the experimental results are given in Section 3. Homogenization is performed in Section 4 to estimate the macroscopic Young's modulus. A discussion about the impact of microstructural attributes and the experimentally studied scale on the macroscopic Young's modulus estimation is conducted in Section 5, before giving the main conclusions in Section 6.

## 2. Materials and Methods

### 2.1. Macroscopic Properties

Six carbonate rocks, denominated from A to F, are considered in this study. The Young's modulus of each rock was measured from triaxial experiments performed at room temperature on cylindrical samples with a 3.8 cm diameter and a 7.6 cm height. The method for Young's modulus measurement, based on an internal standard from Total (now TotalEnergies), was the following. Each sample was equipped with two axial strain gauges and two radial strain gauges and placed in a triaxial cell, which makes it possible to independently control the axial confining stress, the radial confining stress, and the pore pressure. The samples were saturated with brine. The confining stresses were increased isotropically at a rate of 1 bar per minute, together with the pore pressure, up to values close to the in-situ effective stress. During this increase, the difference between the stresses and the pore pressure was kept constant. The samples were then sheared by compressing the sample axially at a rate of 0.01 mm/min. A range over which the relationship between the axial stress and the axial strain was linear was observed for all samples. The Young's modulus was calculated as the slope of this relationship. Besides, the global porosity of each rock was measured using a helium pycnometer. Results are shown in Figure 1.

Although Young's modulus tends to decrease with increasing porosity, these results clearly show that global porosity is not the only factor controlling the elastic behavior. Rocks A, B, and C have very close porosity fractions (around 12%), but exhibit a great dispersion in their Young's moduli (up to a factor of 2.3), even though the first two rocks belong to the same facies F1 (see Figure 1). In addition, although Rocks D and E both have porosity fractions

around 20%, the Young's modulus of Rock D is almost double than that of Rock E. Finally, Rock F belongs to the same facies as that of Rocks A, B, and E, but has the highest porosity fraction. However, its Young's modulus is comparable to that of Rock B and even higher than that of Rock E. Therefore, other parameters than the global porosity are involved in controlling their elastic behavior.

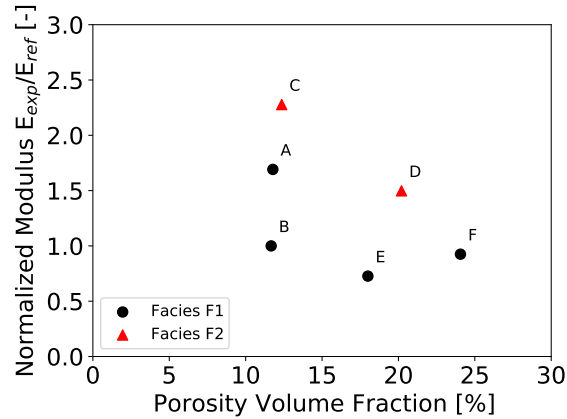


**Figure 1:** Facies and Young's modulus  $E_{exp}$  measured from macroscopic mechanical experiments and normalized by a reference value  $E_{ref}$ , plotted against the porosity volume fraction of several carbonate rocks.

## 2.2. Sample Preparation for Nanoindentation and Microscopy

The calculation of mechanical properties from the indentation response supposes that the sample surface is perfectly flat. Thus, the surface of the studied sample must be prepared cautiously to be as flat and smooth as possible. SEM-EDS observations also require small and smooth samples. Thus, a centimetric-scale piece of each rock was cut using a diamond wire. The samples were then coated with transparent resin (Epofix, Struers). The surfaces of the samples were polished using silicon carbide papers (SiC foil #220; #1200; #2000 and #4000, Struers) in dry conditions at first, and later, using MD-Dur discs made of woven silk (Struers) with 3- $\mu\text{m}$  and 1- $\mu\text{m}$  alcohol-based diamond suspensions without the usage of a lubricant. The entire procedure can be found in the Ph.D. dissertation of Tazi<sup>39</sup>.

In order to provide meaningful results with indentation, the polished surface's roughness must respect a criterion defined in relation with the applied penetration depth of the indenter. The Atomic Force Microscopy (AFM) can be used to evaluate the roughness of a zone on the polished surface<sup>40</sup>. This technique allows characterizing the surface's topography with high resolution, i.e., in the order of fractions of 1 nanometer. AFM characterization was performed on all the samples, and the quadratic roughnesses are found to take values between 21 and 28 nm over  $40 \times 40 \mu\text{m}^2$  sections. These values seem to be in line with those published in the literature<sup>39,41</sup>. The Miller et al.<sup>42</sup> criterion, proposed for cement paste materials, requires a quadratic roughness, evaluated on a square zone of side length  $l$ , such as:

$$\left(R_q^{l \times l}\right)_{l=200 \times \bar{h}} \leq \frac{\bar{h}}{5} \quad (1)$$

where  $\bar{h}$  is the mean penetration depth. For a bone material, Donnelly et al.<sup>43</sup> have found that the measurements of nanoindentation are not affected by the roughness when its value is lower than  $\bar{h}/3$ . In the absence of a criterion developed for rock materials (to our knowledge), the Miller et al.<sup>42</sup> criterion is applied here on the  $40 \times 40 \mu\text{m}^2$  sections and the following lower bound is obtained for the penetration depth:  $\bar{h} > 5 \times 28 = 140 \text{ nm}$ .

## 2.3. Instrumented Nanoindentation Technique

### 2.3.1. Principles

The instrumented nanoindentation technique consists of pressing a hard diamond tip into the studied material<sup>44</sup>. According to Larson et al.<sup>45</sup>, the material domain in which the properties are measured has a characteristic linear

dimension  $L$  estimated at around ten times the penetration depth  $h$  for metals:

$$L \simeq 10 \times h \quad (2)$$

170 Whatever the factor is for rocks, shallower indentations identify the properties of a smaller volume of the material.  
 171 Conversely, deeper indentations measure the properties of larger domains. The test comprises three phases: a  
 172 loading phase followed by a holding phase and an unloading one. A visible imprint is left on the surface of the  
 173 tested material's surface, with a dimension of about 5 to 6 times the maximum penetration depth. Two mechanical  
 174 properties of the material are usually measured from the unloading curve:

1. The indentation modulus  $M$  (also called reduced modulus), which is defined as:

$$M = \frac{\sqrt{\pi}}{2} \frac{S}{\sqrt{A_c}} \quad (3)$$

where  $S = \left( \frac{dF}{dh} \right)_{h=h_{max}}$  is the unloading stiffness at the beginning of the unloading phase and  $A_c$  is the projected contact area at maximum depth. In the case of an ideally sharp Berkovich-type indenter,  $A_c$  can be related to the maximum depth  $h_{max}$  with the Oliver and Pharr<sup>46</sup> method as following:  $A_c = 24.5 \times h_{max}^2$ . The indentation modulus  $M$  is linked to the elastic properties of the indented material (Young's modulus  $E$  and Poisson's ratio  $\nu$ ) and of the indenter ( $E_i$  and  $\nu_i$ ) through the following relation:

$$\frac{1}{M} = \frac{1 - \nu^2}{E} + \frac{1 - \nu_i^2}{E_i} \quad (4)$$

2. The indentation hardness  $H$ , which represents the average pressure below the indenter, is defined as follows:

$$H = \frac{F_{max}}{A_c} \quad (5)$$

175 This parameter is often interpreted as a snapshot of the strength of the material<sup>47,48</sup>.

176 In the present study, quasi-static indentation tests were performed using a NHT<sup>2</sup> nanoindentation tester from CSM  
 177 Instruments (now Anton Paar) and a diamond Berkovich tip ( $E_i = 1140$  GPa,  $\nu_i = 0.07$ ). The tip imperfections  
 178 were taken into consideration by calibrating the contact area  $A_c$  as a function of the penetration depth (using a  
 179 fused silica sample and following the Oliver and Pharr<sup>46</sup> method). Grids of indentation tests were performed, as  
 180 required to identify the properties of individual phases in heterogeneous materials such as rocks<sup>37</sup>.

### 181 2.3.2. Nanoindentation Experiments

182 On each sample, four grids of 40  $\mu\text{m}$ -spaced indentation tests were performed. The grids were carried out in a  
 183 way to cover all the principal mineral phases of the studied material (preselected using SEM). Each grid is formed  
 184 either by  $20 \times 20$  or  $15 \times 15$  tests, covering thus an area of  $760 \times 760 \mu\text{m}^2$  or  $560 \times 560 \mu\text{m}^2$ , respectively. The  
 185 maximum penetration depth was 200 nm, which respects the Miller et al.<sup>42</sup> criterion (see Section 2.2), and is  
 186 sufficiently small to obtain the individual properties of the phases. Each indentation test was performed with a  
 187 loading/unloading rate of 6 mN/min and a holding duration of 10 seconds. All indentation curves were inspected  
 188 visually, and those not sufficiently smooth were removed from the analysis.

189 To find the indented area in the SEM afterward (see Section 2.4), an artificial direct orthogonal frame was created  
 190 with the indenter by performing three large imprints (up to the maximum force 500 mN) next to the sample's  
 191 borders, as shown schematically in Figure 2a. The location of these tests was chosen to facilitate their identification  
 192 in the SEM. In addition, to identify the position of each imprint of a grid accurately, this latter was performed with  
 193 larger imprints at the four corners (see Figure 2b). The corner indentation tests were performed up to a maximum  
 194 force of 40 mN, leaving imprints whose sizes are in the order of 6  $\mu\text{m}$ .

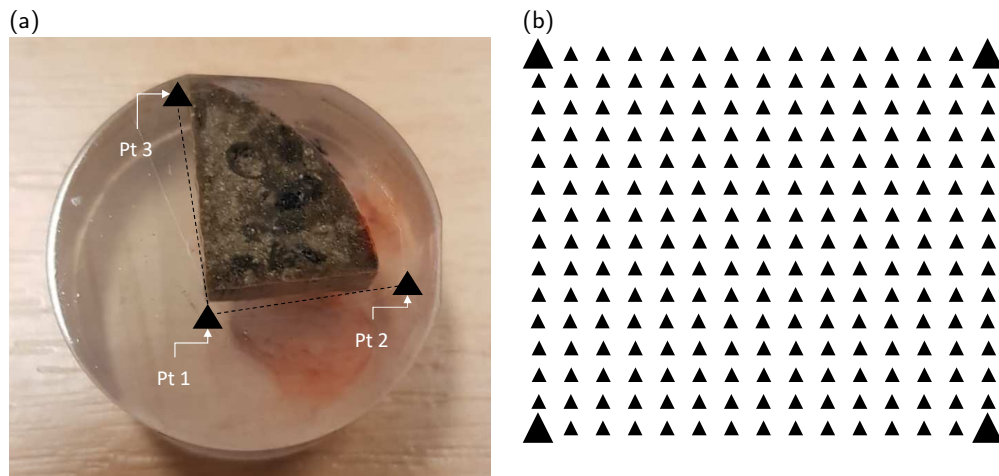


**Figure 2:** (a) Schematic of the direct orthogonal frame formed by 3 indentation tests performed on the sample; (b) Schematic of a typical indentation grid performed with large imprints at the corners.

## 2.4. Coupling Nanoindentation Measurements with SEM-EDS Mapping

### 2.4.1. SEM-EDS measurements

SEM-EDS observations were performed using a MEB-FEG Quanta 650 (FEI) microscope, with an acceleration tension of 15 kV. The minerals were obtained through QEMSCAN (Quantitative Evaluation of Minerals by Scanning Electron Microscopy) methodology, which is based on SEM-EDS elemental mapping. The SEM-EDS hypermaps are post-processed via the Nanomin Software (ThermoFisher), which compares the EDS spectra obtained on each pixel to a mineralogical database previously built according to the nature of the rock (carbonate, sandstone, etc.). The SEM-EDS QEMSCAN method has been shown to be an accurate quantitative tool to characterize mineralogy<sup>49</sup>. The mineralogy of the studied facieses is simple, mainly composed of large grains of calcite and dolomite, and can be clearly identified using the QEMSCAN methodology.

Backscattered SEM images and EDS maps were performed on the zones covered by the indentation grids (see Section 2.4.2 below), with pixel sizes of 100 nm and 1  $\mu\text{m}$ , respectively. The mineral composition of a layer whose thickness is 1  $\mu\text{m}$  is rendered in the EDS maps. Therefore, the data of the latter maps roughly probe the same depth as indentation tests since the characteristic size of the indented domain was around 2  $\mu\text{m}$ .

Finally, EDS mapping of the whole surface of the sample was also performed, with a pixel size of 20  $\mu\text{m}$ , to get a statistically representative characterization of the mineralogical composition. A SEM image of the whole surface was also obtained in backscattered mode by stitching 16 images with a pixel size of 800 nm.

### 2.4.2. Identification of indentation locations in SEM-EDS images

After performing the indentation grids, each sample was inspected with SEM. However, it is complicated, if not impossible, to retrieve the indentation grids in SEM due to the indentations' small size. A two-step procedure was used to locate the indentation positions on the EDS maps, i.e. to identify the mineralogical phase located at each indentation test.

First, the grid's locations on the sample's surface were found based on the known coordinate systems of each experimental device. The coordinates of the three large imprints of the artificial frame defined in Section 2.3.2 (Figure 2a), easily recognizable in SEM images, were determined in the SEM coordinate system. A frame transformation, composed of a translation and a rotation, was then identified to convert the indenter to the SEM coordinate systems<sup>1</sup>. This transformation was used to obtain the coordinates of the grids in the frame of the SEM from their known location in the frame of the indenter. Note that this simple geometric method here permitted

<sup>1</sup>A Python script is written for this purpose. All the Python codes relative to the current study are available for interested readers in the link given at the end of this paper.

identifying indentation grid areas with an accuracy in the order of tens of micrometers. This is essentially due to the fact that the sample is not perfectly horizontal in the SEM.

Second, each indentation's location had to be inferred from the four deeper indentation locations at the corner of the grids. In fact, the imprints left by the 200 nm depth indentations were too small to be identified individually in the SEM. They could be mistaken for micropores or might not even be visible. On the contrary, the deeper indentations at the corners could be easily identified (Figure 3b). The global grid shapes were systematically found to be slightly deformed in the SEM images compared to the square shape performed in the indenter frame, as shown in Figure 3a. A  $20 \times 20$  indentations grid, regularly spaced of  $40 \mu\text{m}$  in the indenter frame, exhibits borders ranging from  $760 \mu\text{m}$  to  $764 \mu\text{m}$  (instead of  $760 \mu\text{m}$ ) and angles varying between  $89^\circ$  and  $91^\circ$ . Therefore, a deformed grid had to be considered to predict all imprints' positions from the four corner positions. The deformation of the grid was assumed to be homogeneous. The mathematical developments of such geometric transformation can be found in Appendix A and were implemented in a Python script. Despite their shallow depth, some nanoindentation imprints could be retrieved in the SEM image presented in Figure 3a and were used to estimate this interpolation procedure's accuracy. Fifteen imprints were chosen randomly in the grid (in the central zone and around each corner), and the error between true imprints' positions and the interpolated ones were manually evaluated (e.g., Figure 3c). The accuracy on the individual imprints positions is found to be lower than  $3.5 \mu\text{m}$ . The maximum error values were observed in the central part of the grid.

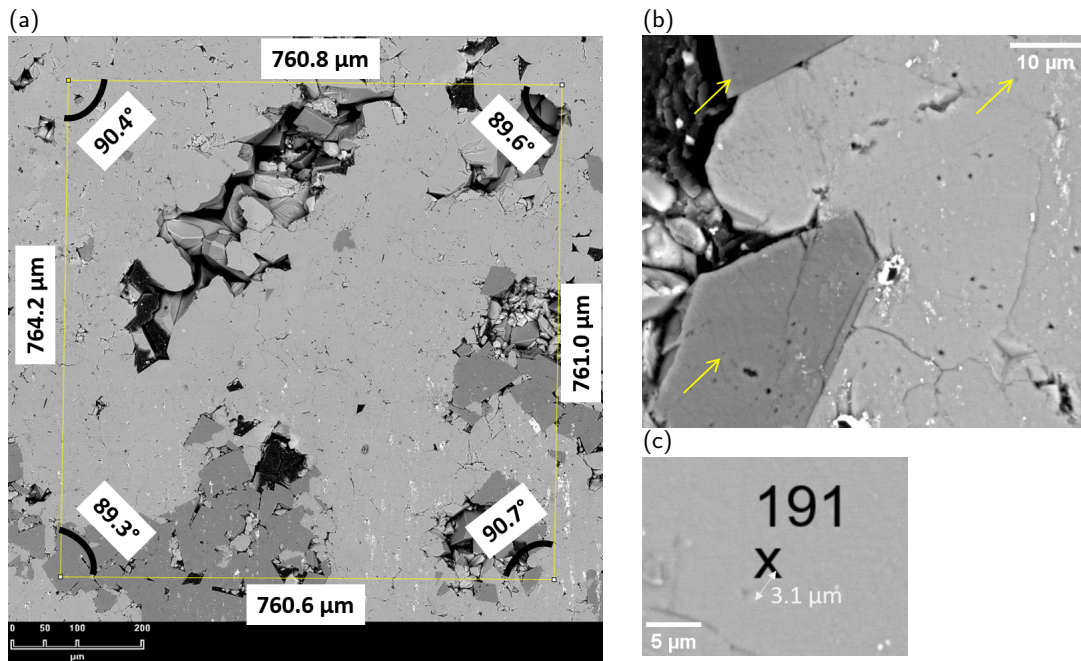


**Figure 3:** (a) SEM image showing the global geometry of an indentation grid of  $20 \times 20$  tests regularly spaced of  $40 \mu\text{m}$  in the indenter frame; (b) Enlargement in the lower right corner, showing the large corner imprint. The arrows point at the locations of the nearest 200 nm depth indentations. (c) SEM image showing the error between the real imprint position of the 191-th indentation of the grid and its position interpolated from those of the 4 deep corner imprints.

#### 2.4.3. Exclusion of indentation tests near interfaces

Once the imprints' positions are found on the SEM and EDS maps, a phase can be attributed to each indentation test. However, to measure the properties of pure phases, the domain probed by an indentation test must be included entirely in a single phase. Therefore, the indentations whose probed volume would overlap two phases must be removed. The Euclidean distance  $d$  of each imprint to the nearest interface between two mineralogical phases has been automatically calculated after segmenting the EDS images (the whole procedure is available in Python language). Then, all the tests having a distance  $d$  lower than a threshold  $d_{th}$  have been excluded from the subsequent analysis. The value of  $d_{th}$  has been chosen to be greater than the sum of the maximum error on an imprint position



(3.5  $\mu\text{m}$ ) and the characteristic size of the probed domain by indentation (around 2  $\mu\text{m}$ ), leading to  $d_{th} = 6 \mu\text{m}$ . Notice that this method does not make it possible to remove indentations whose probed volume would overlap two phases if the second phase is right below the indented surface and not visible on the SEM-EDS images.

## 2.5. Typical Result

A typical result of a fully-studied indentation grid is presented in Figure 4. The grid, having a rectangular shape in the initial configuration ( $20 \times 10$  indentations), covers a zone containing 3 phases. 87% of these 200 tests (i.e., 174 tests) were considered valid by the simple inspection of their force-penetration curves and retained in the subsequent procedure. The EDS map indicates that the matrix phase is formed with calcite, and many inclusions of dolomite and anhydrite phases are observed (dark grey and white color in the SEM image, respectively). The distance threshold has been applied to identify the indentations that would have probed a single phase, leading to a selection of only 87 tests, which are sorted by phase. Finally, the corresponding distributions of the indentation modulus  $M$  and hardness  $H$  are given in Figures 4c and 4d. For the various performed indentation grids, these histograms will be henceforth directly given for the sake of conciseness.

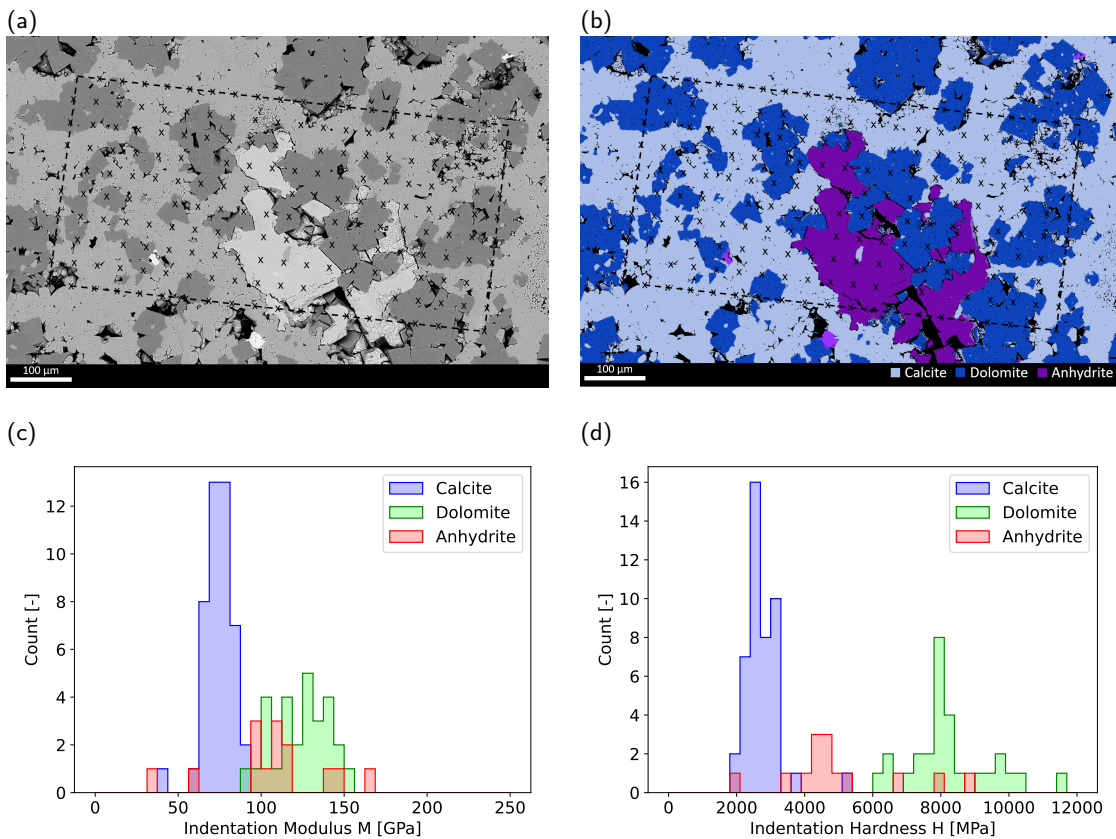


**Figure 4:** (a) Example of a SEM image over which the indentation grid is superimposed ; (b) Corresponding EDS map. Each cross stands for the location of one indentation test and the contour of the grid is marked here with dashed lines; (c)-(d) Histogram of the properties  $M$  and  $H$  of the identified phases: matrix of calcite with inclusions of dolomite and anhydrite.

## 3. Experimental Results

### 3.1. Microstructure's Characterization

As shown in Figure 5, a continuous calcite phase is identified in the rocks belonging to Facies F1: Rocks A, B, E, and F. Different mineral phases can be observed in this phase, such as dolomite and anhydrite (Rocks A

**Table 1**

Volume fractions of the rocks' phases evaluated from the EDS maps performed on the whole surfaces, and porosities measured from MIP tests. The mineral fractions are expressed with respect to the total volume. All values are rounded to 0.1%.

Rock	Calcite	Dolomite	Anhydrite	Quartz	$\phi_{macro}$	$\phi_{micro}$
Rock A	67.0%	19.9%	1.3%	0.0%	7.1%	4.7%
Rock B	70.5%	14.1%	3.7%	0.0%	5.8%	5.9%
Rock C	0.4%	72.6%	14.6%	0.0%	10.5%	1.9%
Rock D	0.0%	76.1%	3.7%	0.0%	13.3%	6.9%
Rock E	79.0%	0.0%	0.0%	3.0%	9.4%	8.6%
Rock F	74.1%	0.0%	0.0%	1.8%	N/A	N/A

and B), or quartz only (Rocks E and F). Figures 6, 7 and 8 present several SEM observations performed on the samples of Rock A to Rock F. In Rock A, large pores are observed at the millimeter scale, as well as isolated subspherical dolomite inclusions marked with the letter **D**. Besides, some anhydrite traces (marked by the letter **A**) are embedded in the calcite matrix. At lower scales, a family of micropores is observed in calcite (Figure 6d). In contrast, dolomite and anhydrite are quite more compact (Figures 6c and 6d). The diameters of micropores are at the scale of 1  $\mu\text{m}$ , whereas macropores exhibit diameters ranging from several tens of micrometers up to the scale of 1 mm. As for Rock B, the dolomite phase seems to be less present and less homogeneously distributed in the volume space (Figure 5b) than in Rock A. The SEM observations on Rock B shown in Figures 6e and 6f suggest the presence of two porosity families again: micropores in the calcite phase and macropores at a larger scale. Anhydrite and dolomite seem to be quite compact. Besides, the SEM observations on Rock E and F presented in Figure 8 make evidence of large subspherical macropores lying in the calcite matrix and a family of micropores at the scale of several micrometers. Minor traces of quartz are identified in the EDS maps performed on the whole surfaces of both Rocks E and F (Figures 5e and 5f).

On the other hand, Rocks C and D, which belong to Facies F2, exhibit a completely different microstructure (Figures 5c and 5d). Dolomite grains are found to form the major phase of these two rocks. In Rock C, subspherical grains of dolomite are identified (Figures 7a and 7b). An anhydrite cementation is found among the grains in some zones, and an intergranular porosity without evidence of cementation is observed in others. Unlike anhydrite, the dolomite phase is observed to contain a family of micropores. In addition, a small proportion of calcite is identified on the EDS map. However, the SEM observations performed on Rock D show the presence of angular crystals of dolomite (Figures 7c and 7d). Moreover, anhydrite is less present in this rock, as only minor isolated traces are identified. Besides, no calcite phase has been observed in the EDS map of this rock.

The mineral phases' surface fractions are evaluated from the EDS maps carried out on the samples' whole surfaces (Figure 5). These fractions are assumed here to be equivalent to the volume fractions with respect to the total volume (following Delesse<sup>50</sup>). Since EDS probes only the solid skeleton, those volume fractions are measured with respect to the volume of the solid skeleton. We then multiply those volume fractions by  $(1 - \phi)$  (where  $\phi$  is the total volume fraction porosity assessed by MIP), to obtain mineral volume fractions expressed with respect to the total volume of the sample. Results are gathered in Table 1. Calcite forms the major phase in the rocks belonging to Facies F1, whereas dolomite is the major phase in the rocks of Facies F2. Between Rocks A and B, dolomite is more present in the former. Minor traces of anhydrite are identified in both rocks (less than 4%). In contrast, Rocks E and F exhibit only the minor presence of quartz inclusion. For Facies F2, anhydrite is more present in Rock C than in Rock D. No calcite is identified in Rock D, whereas only 0.4% of calcite is found in Rock C.



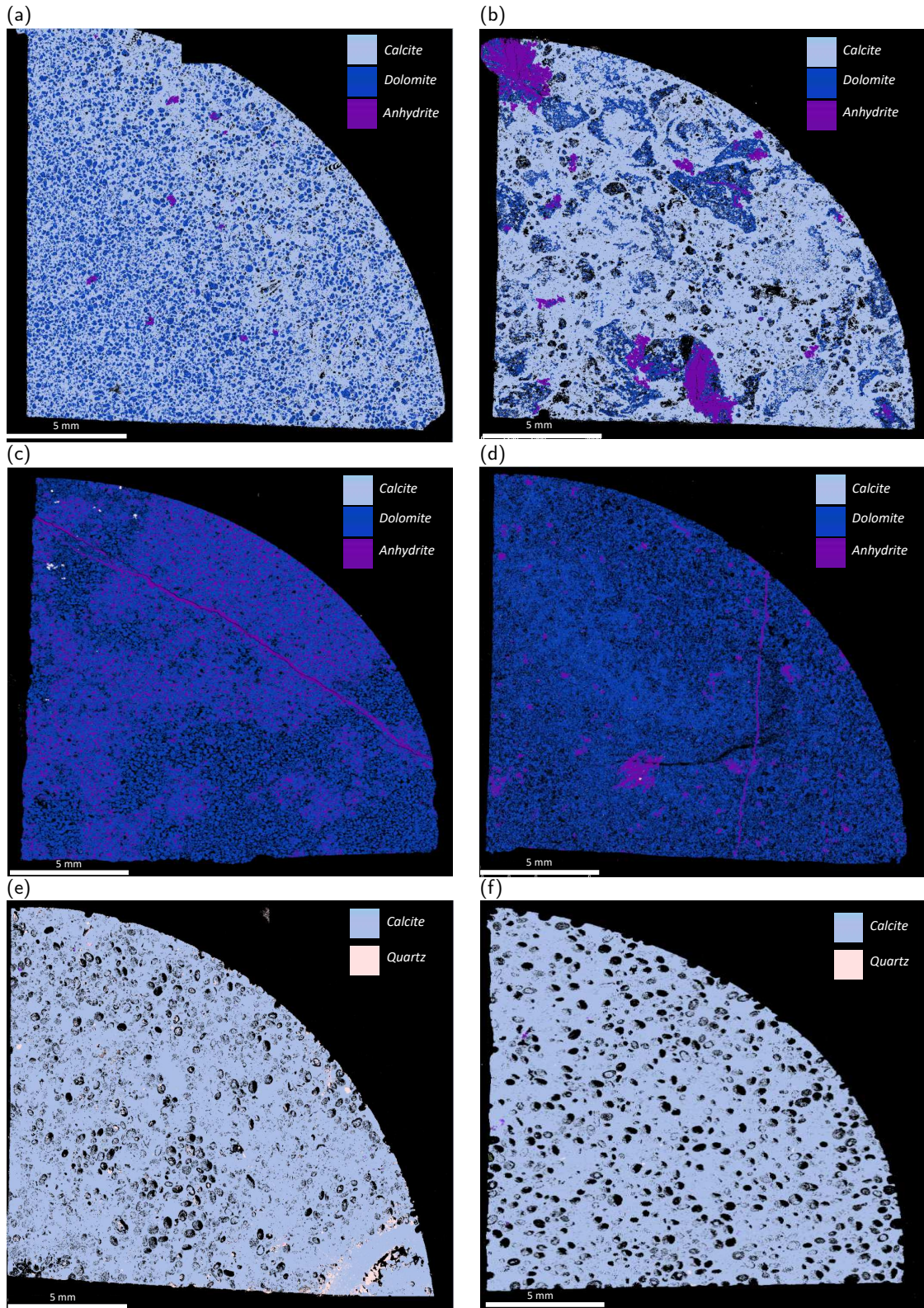
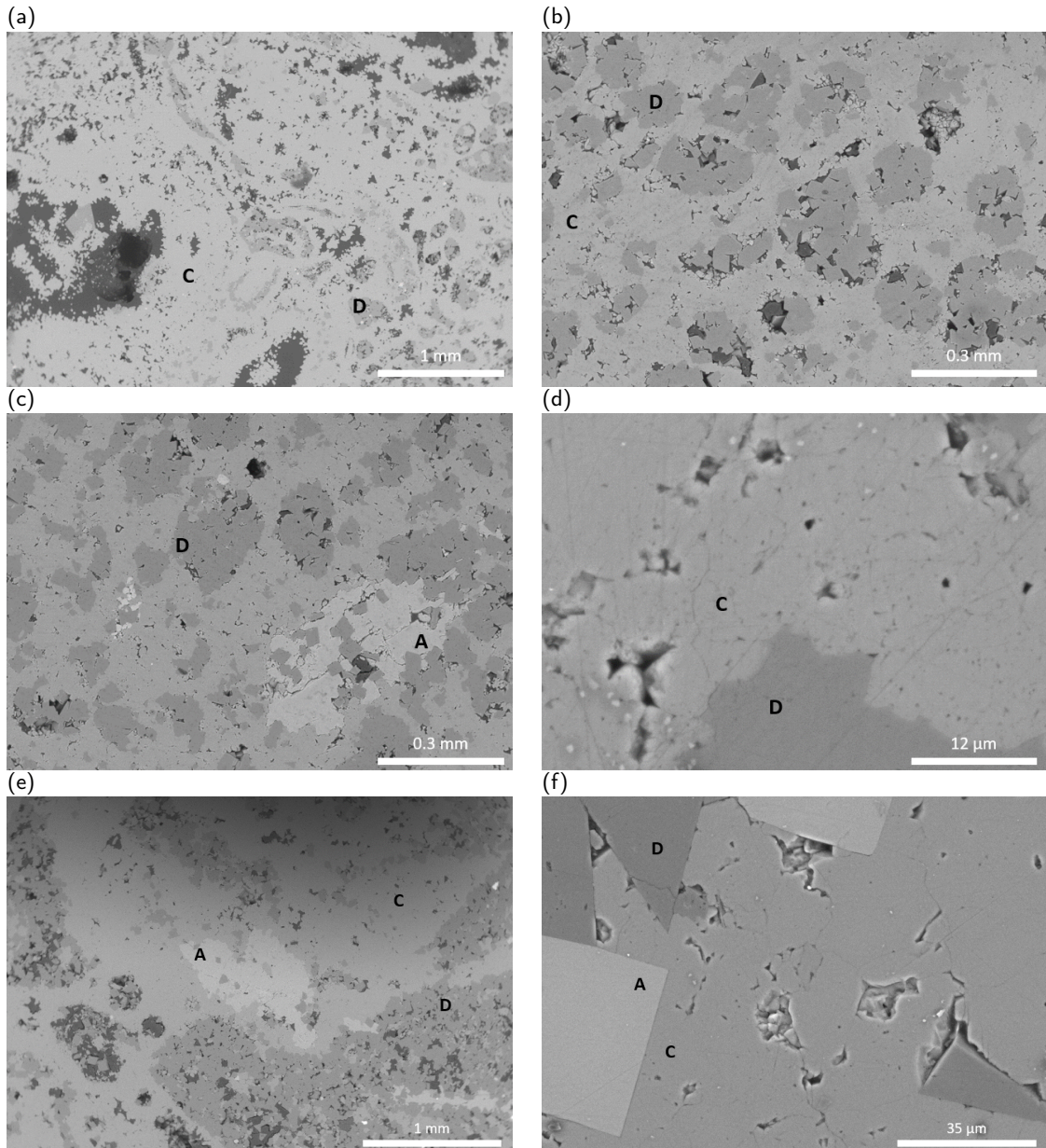
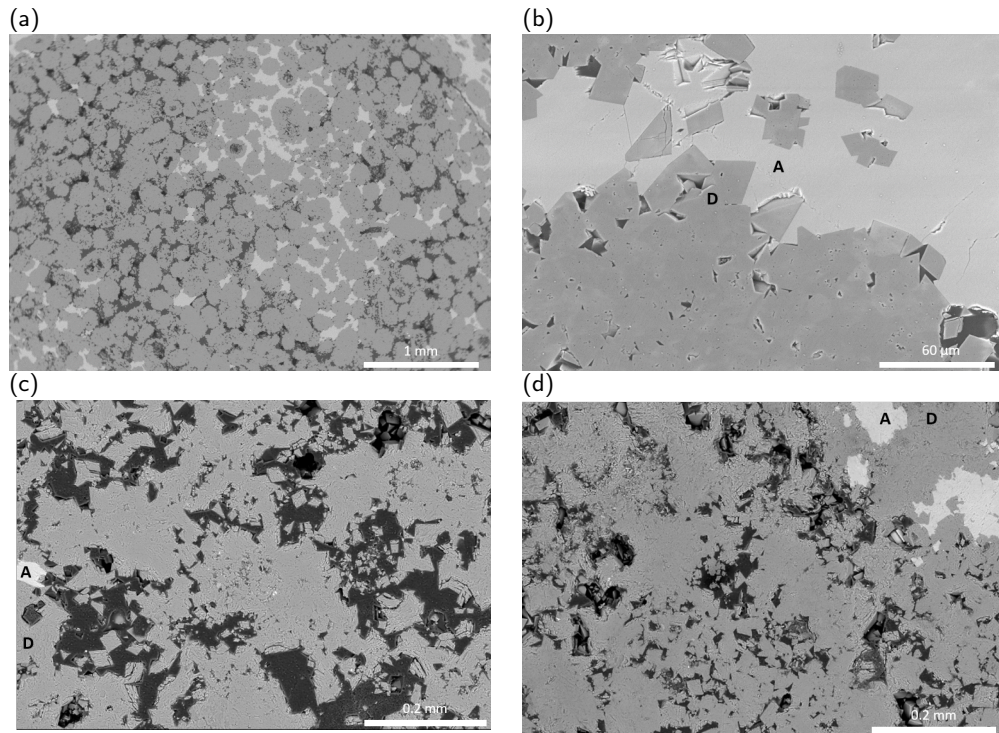


Figure 5: EDS maps performed on the whole surface of the samples: (a-f) Rocks A to F.





**Figure 6:** Backscattered SEM observations of: (a-d) Rock A; (e-f) Rock B. The letters C, D and A denote calcite, dolomite and anhydrite, respectively.



**Figure 7:** Backscattered SEM observations of: (a-b) Rock C; (c-d) Rock D. The letters D and A denote dolomite and anhydrite, respectively.

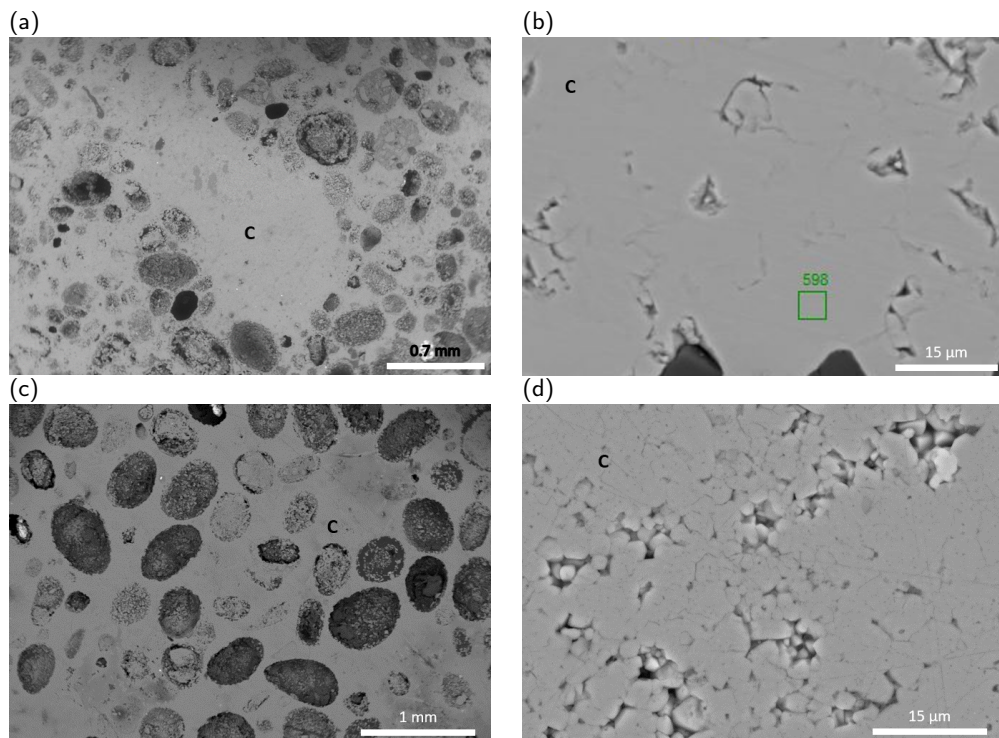


**Figure 8:** Backscattered SEM observations of: (a-b) Rock E; (c-d) Rock F. The letter C denotes calcite.

Moreover, MIP tests have been conducted on samples cored from Rocks A to E to evaluate the porosity families' volume fractions (Figure 9). Unfortunately, the sample of Rock F that we possess had been already tested mechanically (to measure its macroscopic Young's modulus), and its microstructure had been thus deformed. Therefore, MIP has not been performed on a sample from this rock. Note that the total porosities of the samples provided in Table 1 are close to the one displayed in Figure 1 and obtained by helium pycnometry on companion samples: this good agreement suggests that our samples are representative.

The MIP curves of Rocks A to C, which have global porosities around 12%, are gathered in Figure 9a. The dominant pore size is in the 10  $\mu\text{m}$  range for Rocks A and C. We observe no clear peak for Rock B, whose pore size distribution extends from 0.1 to 10  $\mu\text{m}$ . Figure 9b shows the MIP results corresponding to Rocks D and E, whose global porosities are between 18% and 20%. The MIP curves of Rock D and E exhibit peaks at 0.5  $\mu\text{m}$  and 3  $\mu\text{m}$ , respectively. It is worth mentioning that at a given global porosity, the rock which contains more microporosity is the one whose Young's modulus is the lowest (Rock B in Figure 9a and Rock E in Figure 9b). This result is in agreement with the results published by Weger et al.<sup>7</sup>.

For modeling purposes, we will need the volume fraction of the various porosity families. Based on the microstructural observations and the MIP measurements presented above, we introduce a threshold diameter between microporosity and macroporosity and set it to 2  $\mu\text{m}$  for all the studied rocks. Accordingly, the volume fractions of the porosity families are given in Table 1. The impact of the value of this threshold on the homogenized mechanical properties will be discussed in Section 4.3.

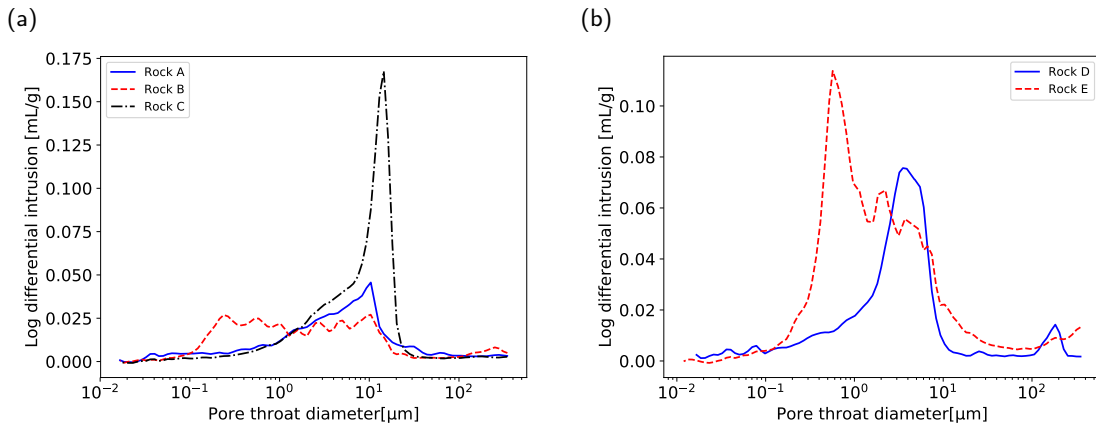


**Figure 9:** Results of MIP conducted on samples extracted from Rocks A to E.



**Table 2**

Mean values ( $\mu_M$  and  $\mu_H$ ) and standard deviations ( $\sigma_M$  and  $\sigma_H$ ) of, respectively, the indentation modulus and hardness obtained for the rocks' solid phases.

Rock	Calcite		Dolomite		Anhydrite	
	$\mu_M \pm \sigma_M$ [GPa]	$\mu_H \pm \sigma_H$ [GPa]	$\mu_M \pm \sigma_M$ [GPa]	$\mu_H \pm \sigma_H$ [GPa]	$\mu_M \pm \sigma_M$ [GPa]	$\mu_H \pm \sigma_H$ [GPa]
Rock A	75.1 $\pm$ 11.6	2.8 $\pm$ 0.6	125.5 $\pm$ 15.8	8.4 $\pm$ 1.2	107.1 $\pm$ 31.6	5.0 $\pm$ 1.7
Rock B	63.3 $\pm$ 17.8	2.4 $\pm$ 0.7	105.4 $\pm$ 24.0	5.7 $\pm$ 1.7	91.3 $\pm$ 24.0	3.4 $\pm$ 0.6
Rock C			130.6 $\pm$ 16.1	7.4 $\pm$ 1.1	108.5 $\pm$ 16.9	4.0 $\pm$ 0.7
Rock D			105.9 $\pm$ 15.7	5.1 $\pm$ 1.0		
Rock E	48.4 $\pm$ 11.6	1.7 $\pm$ 0.7				
Rock F	59.4 $\pm$ 10.7	1.7 $\pm$ 0.6				

### 3.2. Local Mechanical Properties

Nanoindentation experiments have been conducted following the procedure presented in Section 2. The corresponding histograms of the indentation modulus  $M$  and hardness  $H$  classified by phases for Rocks A to C and Rocks D to F are given in Figures 10 and 11, respectively. The mean values  $\mu$  and standard deviations  $\sigma$  of the indentation properties of the rocks' mineral phases are then calculated and listed in Table 2. Dolomite is found to be the stiffest and hardest phase in comparison with calcite and anhydrite, as its indentation modulus's mean values  $\mu_M$  vary between 105.4 and 130.6 GPa and its indentation hardness's mean values  $\mu_H$  vary between 5.1 and 8.4 GPa. Calcite is the softest phase, with  $48.4 < \mu_M < 75.1$  GPa, and  $1.7 < \mu_H < 2.8$  GPa. The properties of calcite in Rock E are lower than in the rocks of Facies F1, which may explain its lower value of Young's modulus (Figure 1). Anhydrite has intermediate properties with  $91.3 < \mu_M < 108.5$  GPa, and  $3.4 < \mu_H < 5.0$  GPa. When a phase is rarely present in the microstructure, its properties may sometimes not be measured from nanoindentation grids, as is the case for calcite in Rock C, anhydrite in Rock D, and quartz in Rocks E and F. The obtained results are consistent with those measured by Tazi<sup>39</sup>, who has studied a source rock and obtained the following properties for calcite:  $70.1 < \mu_M < 73.0$  GPa and  $\mu_H = 2.5$  GPa, and for dolomite:  $97.0 < \mu_M < 107.0$  GPa and  $5.8 < \mu_H < 6.4$  GPa.

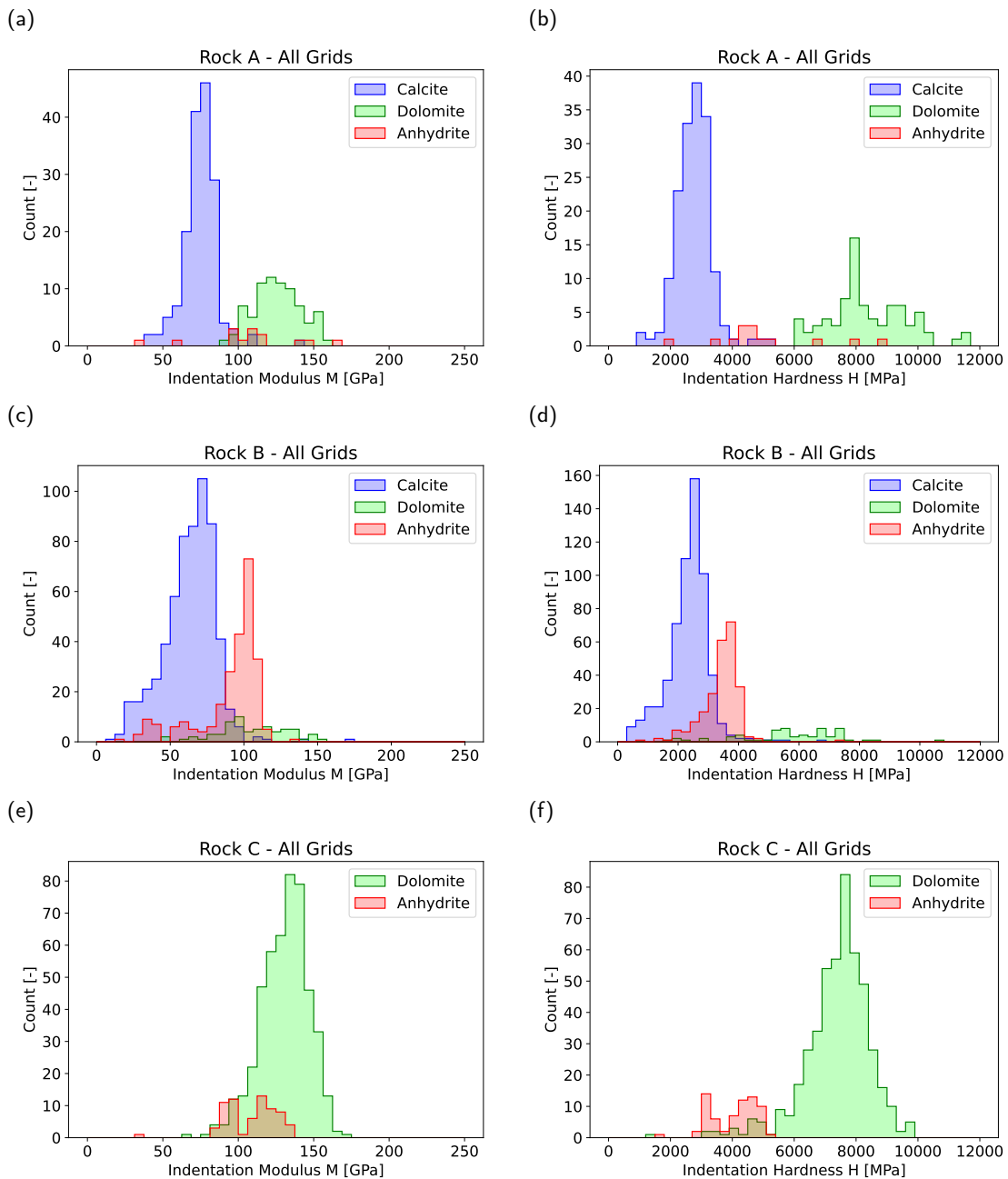


**Figure 10:** Histograms of the indentation modulus  $M$  and hardness  $H$  obtained from all the grids performed on the sample of (a)-(b) Rock A; (c)-(d) Rock B; (e)-(f) Rock C.

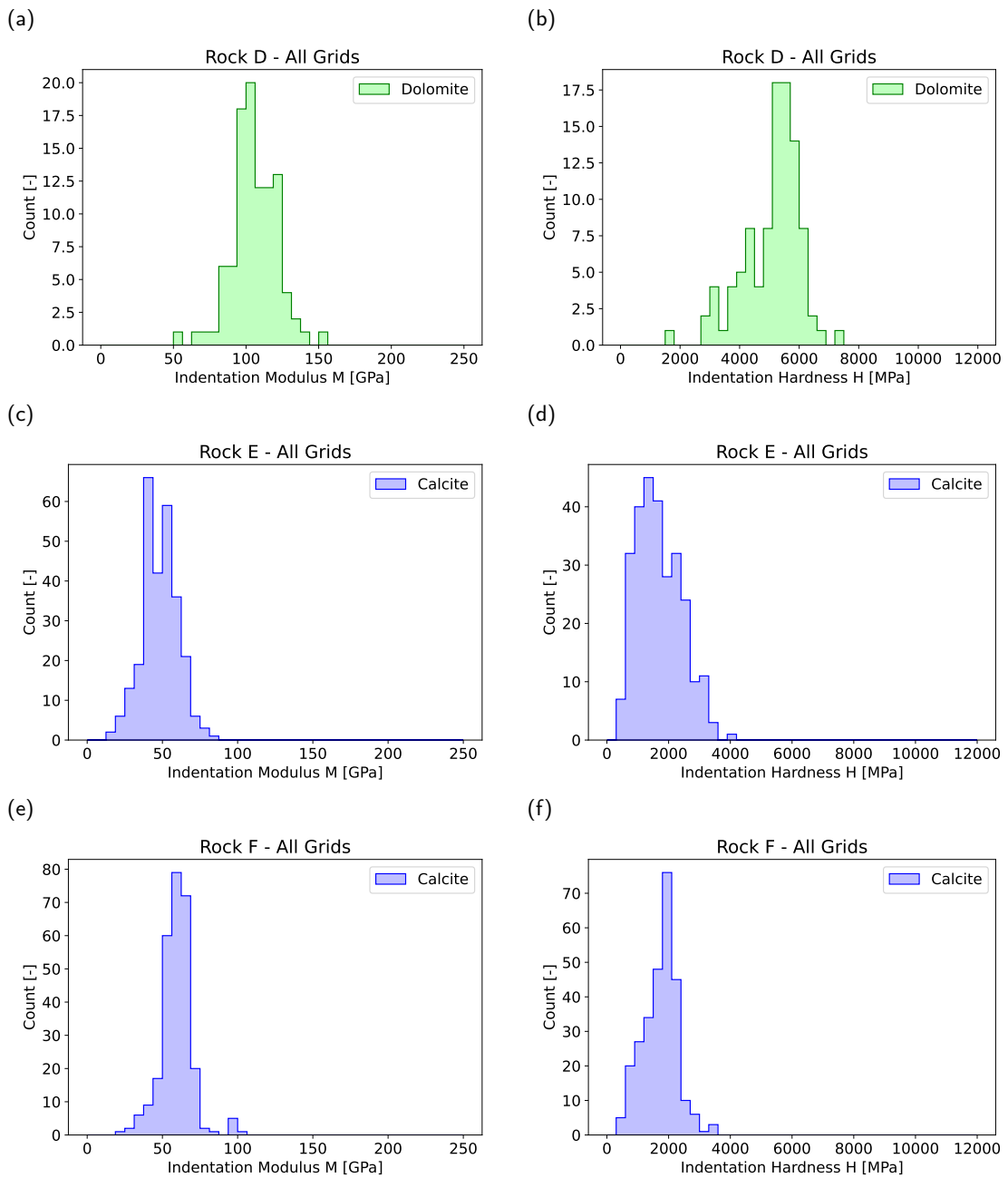


**Figure 11:** Histograms of the indentation modulus  $M$  and hardness  $H$  obtained from all the grids performed on the sample of (a)-(b) Rock D; (c)-(d) Rock E; (e)-(f) Rock F.



**Table 3**

Volume fractions ( $f_i$ ), mean values ( $\mu_M$  and  $\mu_H$ ) and standard deviations ( $\sigma_M$  and  $\sigma_H$ ) of indentation modulus  $M$  and hardness  $H$  for each phase identified in all grids performed on rocks A, B and C, obtained from the SEM-EDS analysis (EDS) and from the deconvolution procedure (dec). Volume fractions are rounded to 0.1%. Volume fractions indicated for the SEM-EDS analysis are the fraction of indentation tests associated to each mineral as obtained from the combined procedure described in section 2.4 and shown in Figure 10.

Rock		Phase 1 - Calcite			Phase 2 - Anhydrite			Phase 3 - Dolomite		
		$f_i$ [%]	$\mu_M \pm \sigma_M$ [GPa]	$\mu_H \pm \sigma_H$ [GPa]	$f_i$ [%]	$\mu_M \pm \sigma_M$ [GPa]	$\mu_H \pm \sigma_H$ [GPa]	$f_i$ [%]	$\mu_M \pm \sigma_M$ [GPa]	$\mu_H \pm \sigma_H$ [GPa]
A	EDS	64.0	75.1 $\pm$ 11.6	2.8 $\pm$ 0.6	5.5	107.1 $\pm$ 31.6	5.0 $\pm$ 1.7	30.4	125.5 $\pm$ 15.8	8.4 $\pm$ 1.2
	dec	53.2	70.9 $\pm$ 10.6	2.5 $\pm$ 0.7	16.9	97.9 $\pm$ 16.4	5.4 $\pm$ 1.2	29.9	130.6 $\pm$ 16.3	8.6 $\pm$ 1.8
B	EDS	65.9	63.3 $\pm$ 17.8	2.4 $\pm$ 0.7	27.1	91.3 $\pm$ 24.0	3.4 $\pm$ 0.6	7.0	105.4 $\pm$ 24.0	5.7 $\pm$ 1.7
	dec	88.0	66.5 $\pm$ 20.9	2.5 $\pm$ 0.7	9.6	104.7 $\pm$ 5.3	5.4 $\pm$ 1.2	2.4	140.1 $\pm$ 23.7	8.6 $\pm$ 1.8
C	EDS				12.4	108.5 $\pm$ 16.9	4.0 $\pm$ 0.7	87.6	130.6 $\pm$ 16.1	7.4 $\pm$ 1.1
	dec				38.2	101.1 $\pm$ 20.2	5.0 $\pm$ 1.4	61.8	134.4 $\pm$ 13.1	7.6 $\pm$ 0.7

### 3.3. Critical Analysis of the Deconvolution Technique

If no SEM-EDS mapping is performed after indentation, the deconvolution technique may be applied to estimate the mineral phases' volume fractions and their indentation properties. This paragraph is devoted to present a critical analysis of this technique in light of the results obtained from coupling nanoindentation and SEM-EDS imaging. The deconvolution technique is applied on the cumulative histograms of indentation modulus  $M$  and hardness  $H$  obtained for rocks A, B and C by following the deconvolution procedure of Ulm et al.<sup>10</sup> : we fit a normal distribution to each property of each phase, by preventing overlapping of the peaks. Therefore, 5 quantities are sought for each phase: its volume fraction  $f_i$ , the mean values  $\mu_M$  and  $\mu_H$  and the standard deviations  $\sigma_M$  and  $\sigma_H$ . The indentation tests considered for this technique are those selected after inspecting their force-penetration curves (i.e., the first stage of test selection presented in Section 2.3.2 prior to the MEB-EDS characterization). In each of the deconvolution analyses, the number of phases imposed corresponds to the one identified with SEM-EDS imaging, i.e. 3 and 2 phases for rocks A/B and rock C, respectively. For rocks A and B, the initial guess parameters of the minimization procedure were set to  $\mu_M = (70, 100, 125)$  GPa and  $\mu_H = (2.5, 6, 8)$  GPa for phases (1, 2, 3), respectively. For rock C, they were set to  $\mu_M = (100, 125)$  GPa and  $\mu_H = (5, 8)$  GPa for phases (1, 2). In all cases, a relative standard deviation of 0.3 has been considered for both  $M$  and  $H$  distributions, as well as equal volume fractions for all phases.

Figure 12 and Table 3 display the results obtained for the three rocks. The following conclusions can be made:

1. For the three rocks, although the orders are respected, most deconvoluted volume fractions differ from the ones estimated after SEM-EDS characterization.
2. Depending on the histograms, the deconvolution can lead to mean mechanical properties that differ significantly from the coupled approach using SEM-EDS characterization, i.e. up to 33% for the indentation modulus (rock B, dolomite) and up to 60% for the indentation hardness (rock B, anhydrite). In such cases, coupling SEM-EDS measurements with the nanoindentation data is required to obtain accurate measurements of the mechanical properties.

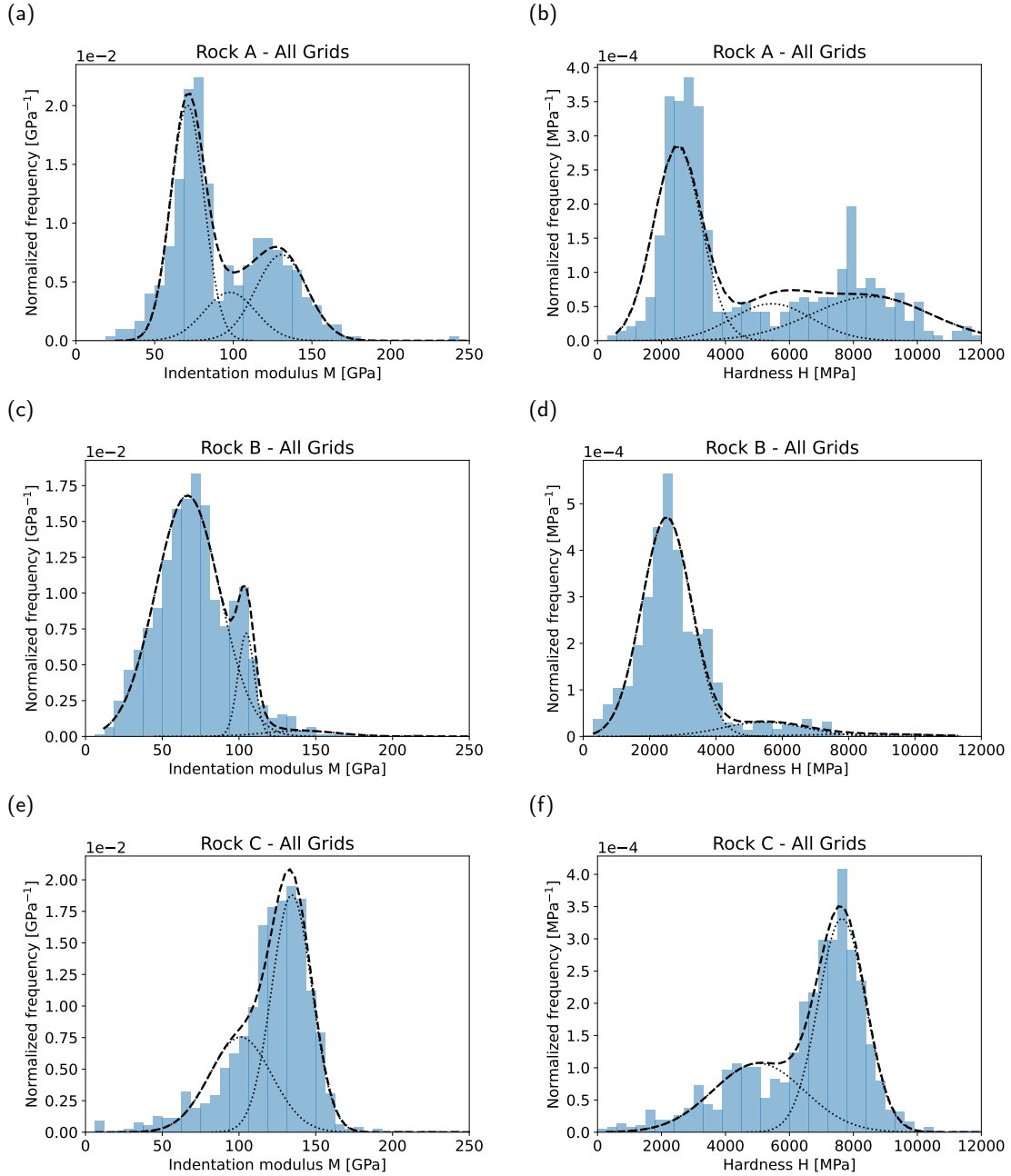


**Figure 12:** Histograms of indentation modulus  $M$  and hardness  $H$  for all grids performed on (a-b) Rock A, (c-d) Rock B and (e-f) Rock C, and corresponding analyses with the deconvolution method. The dashed lines represent the summation of normal distributions weighted by the volume fractions, and the dotted ones represent the individual phase distributions.

## 4. Homogenization of the Young's Moduli

The homogenization theory is applied on the experimental results presented in the previous section to estimate the macroscopic values of Young's modulus of each rock.

### 4.1. Homogenization Principles

The homogenization theory consists of modeling a heterogeneous material with a homogeneous one, which behaves globally in the same way<sup>51</sup>. In our case, we are interested in modeling the elastic behavior of rocks having different microstructures with equivalent homogeneous media in terms of the bulk and shear moduli:  $K$  and  $G$ . In this theory's frame, the homogenized elastic properties depend on each phase's elastic properties forming the microstructure, their volume fractions, and morphologies. In the case of an Eshelbian type morphology<sup>52</sup>, where the phases of the heterogeneous medium are assumed to have ellipsoidal shapes, two main schemes exist in the literature:

1. The Mori-Tanaka scheme<sup>53</sup>, where the main phase is assumed to form a continuous matrix in the material.
2. The self-consistent scheme<sup>54</sup>, which corresponds to polycrystal materials, where none of the phases forms a real continuous phase.

In the case of a Mori-Tanaka scheme, the homogenized bulk and shear moduli of a medium formed by a matrix (index 1) and  $n - 1$  phases (index 2 to  $n$ ) with a spherical shape are respectively expressed as<sup>51</sup>:

$$K_{hom}^{MT} = \left( \sum_{j=1}^n \frac{K_j f_j}{1 + \alpha_1 \left( \frac{K_j}{K_1} - 1 \right)} \right) \left( \sum_{i=1}^n \frac{f_i}{1 + \alpha_1 \left( \frac{K_i}{K_1} - 1 \right)} \right)^{-1} \quad (6)$$

$$G_{hom}^{MT} = \left( \sum_{j=1}^n \frac{G_j f_j}{1 + \beta_1 \left( \frac{G_j}{G_1} - 1 \right)} \right) \left( \sum_{i=1}^n \frac{f_i}{1 + \beta_1 \left( \frac{G_i}{G_1} - 1 \right)} \right)^{-1} \quad (7)$$

where  $f_i$ ,  $K_i$  and  $G_i$  represent the volume fraction, bulk and shear moduli of a phase  $i$  respectively,  $\alpha_1 = 3K_1/(3K_1 + 4G_1)$ , and  $\beta_1 = 6(K_1 + 2G_1)/[5(3K_1 + 4G_1)]$ . In this case, the index 1 refers to the matrix phase. As for the self-consistent scheme, the homogenized moduli for a  $n$ -phases material with spherical shapes have the following expressions<sup>51</sup>:

$$K_{hom}^{SC} = \sum_{i=1}^n \frac{K_i f_i}{1 + \alpha_{hom} \left( \frac{K_i}{K_{hom}^{SC}} - 1 \right)} \quad (8)$$

$$G_{hom}^{SC} = \sum_{i=1}^n \frac{G_i f_i}{1 + \beta_{hom} \left( \frac{G_i}{G_{hom}^{SC}} - 1 \right)} \quad (9)$$

with  $\alpha_{hom} = 3K_{hom}^{SC}/(3K_{hom}^{SC} + 4G_{hom}^{SC})$  and  $\beta_{hom} = 6(K_{hom}^{SC} + 2G_{hom}^{SC})/[5(3K_{hom}^{SC} + 4G_{hom}^{SC})]$ .

The self-consistent indentation technique is an alternative approach proposed by Randall et al.<sup>55</sup> to estimate the homogenized elastic properties of a material directly from a grid of indentation measurements without the need of SEM-EDS analyses. This approach assumes that each indentation test is representative of a material phase, and an equivalent "virtual" composite material, composed of  $n$  randomly and equivalently distributed phases, can be defined. The number of phases  $n$  is identical here to the total number of indentation tests. In such a medium, none of the phases can play a matrix's role, and thus, a polycrystal morphology seems to be well-suited. Therefore, we adopt the self-consistent scheme to calculate the homogenized elastic moduli (Equations 8 and 9).

## 4.2. Homogenization Strategy Inferred From Observations

Based on the microscopic observations presented in Section 3.1, a two-scale scheme is proposed to describe the microstructure of the rocks belonging to Facies F1 and is illustrated in Figure 13a. At the largest scale, a continuous calcite phase containing dolomite, anhydrite, quartz, and macropores is assumed. At the lowest scale, microporous calcite is considered. Another two-scale scheme is proposed to describe the microstructure of the rocks belonging to Facies F2 and is illustrated in Figure 13b. At the largest scale, a dolomite phase containing anhydrite, calcite, and macropores is considered. At the lowest scale, dolomite is considered to be microporous. In-between micropores, both calcite and dolomite could contain nanopores at the scale below (i.e., less than 100 nm). Nanoindentation provides measurements that include the impact of those nanopores on the mechanical properties of the mineral phases. The MIP measurements show the volume of those nanopores to be negligible compared to the total pore volume (Figure 9).

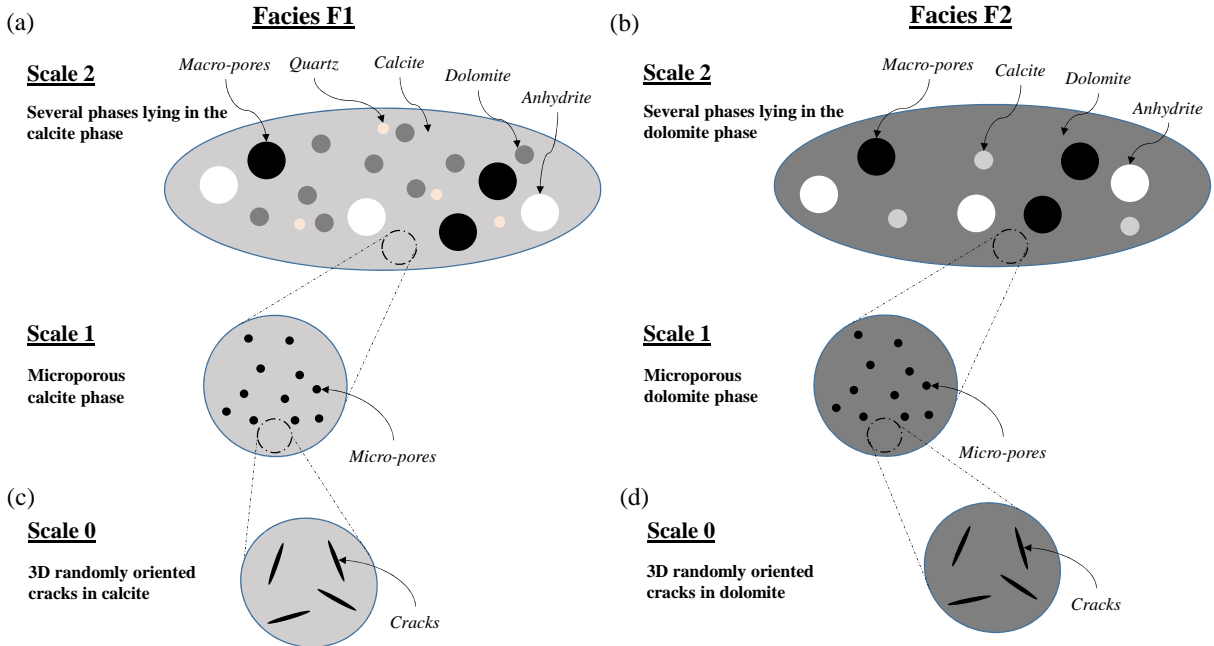


**Figure 13:** (a)-(b) Two-scale schemes proposed to describe the microstructures of the rocks belonging to Facies F1 and F2, respectively; (c)-(d) Additional lower scale introducing 3D-randomly oriented elliptic cracks in the dominant phase of the rocks belonging to Facies F1 and F2, respectively.

The homogenization technique is then applied on the two-scale schemes, taking into account the volume fractions of the different phases and porosity families given in Table 1, and their local properties presented in Table 2 (see also Equation 4). We consider a Poisson's ratio  $\nu = 0.3$  for all minerals, except for quartz, for which  $\nu = 0.08$ <sup>56</sup>. Finally, due to the lack of data on the following phases, some assumptions have been made:

- The properties of calcite in Rock C are taken identical to those obtained for Rock A.
- The properties of anhydrite for Rock D are taken identical to those obtained for Rock C.
- The properties of quartz are taken from Tazi<sup>39</sup>:  $M = 97.0$  GPa to calculate the homogenized modulus of Rocks E and F.
- The total porosity of Rock F is assumed to be equally distributed between macroporosity ( $\phi_{macro}$ ) and microporosity ( $\phi_{micro}$ ).

Note that those assumptions on the mineral properties have little impact on the calculated homogenized modulus since the volume fraction of those phases is 3.7% at most (see Table 1). The effect of the last assumption is discussed in the next section.

### 4.3. Homogenization Results

The homogenized Young's moduli,  $E_{hom}^{MT}$  and  $E_{hom}^{SC}$ , are calculated by considering Mori-Tanaka (Equations 6 and 7) and self-consistent schemes (Equations 8 and 9), respectively. The ratios of these moduli with respect to the experimental values obtained from macroscopic mechanical tests are presented in Figure 14. These plots show that the global trend of Young's modulus is captured in the sense that the homogenized moduli are roughly proportional to the measured ones. In other words, the homogenization technique, fed with the data obtained from coupling nanoindentation and SEM-EDS analyses, can predict if a rock is stiffer than another one. These results suggest that the rock's mineral composition and properties are key parameters governing the elastic behavior and are responsible for the dispersion of Young's moduli presented in Figure 1. However, we observe that the homogenized moduli predicted with upscaling models overestimate the one measured with macroscopic experiments, using both Mori-Tanaka and self-consistent models. The mean overestimation factor is 1.78 for Mori-Tanaka and 1.72 for self-consistent schemes, and their standard deviations are 0.23 and 0.24, respectively. Despite that this factor is lower in the latter case, various homogenization schemes yield quite similar moduli, suggesting that the phases' spatial organization with respect to each other does not seem to have a significant impact on the homogenized moduli.

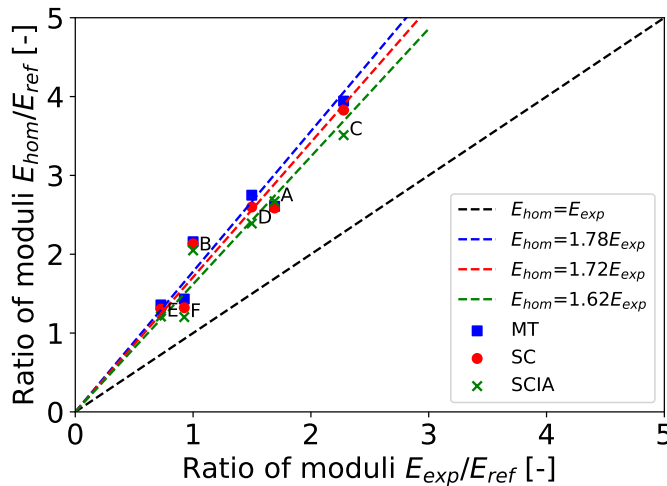


**Figure 14:** Comparison of the homogenized moduli with the macroscopic experimental ones of the six studied rocks, all normalized with a reference value  $E_{ref}$ . Homogenization is performed using Mori-Tanaka (MT) and self-consistent (SC) models, and through the self-consistent indentation approach (SCIA).

To explore the impact on the homogenized moduli of the threshold diameter between microporosity and macroporosity, we vary the threshold over the whole diameter range (Figure 9). In other words, the whole range of porosity distribution between macro and microporosity is explored, leading to the relative errors for each rock given in Figure 15. For the Mori-Tanaka model, the error is lower than 3% for all the rocks. In contrast, these errors are slightly higher using the self-consistent model - as expected - and can reach 6.7% as for Rock F. In conclusion, the impact of the assumption of the diameter threshold on the homogenized moduli is not found to be significant. The sensitivity to Poisson's ratios is studied by varying their value from 0.25 to 0.35 for the three major minerals (calcite, dolomite, anhydrite). For both Mori-Tanaka and self-consistent schemes, the maximum error is about  $\pm 3\%$ , which is also not significant.

Finally, the homogenization has been performed using the self-consistent indentation approach proposed by Randall et al.<sup>55</sup>. To do so, for every single sample, all the nanoindentation tests were gathered from all the grids. Only those having suitable shapes for their force-penetration curves were retained (i.e., the first stage of test removal presented in Section 2.5). These retained tests are assumed to represent the solid phases of the rock. At the location of each indent, we assume a Poisson's ratio  $\nu = 0.3$ , which is the Poisson's ratio of all minerals but quartz. The

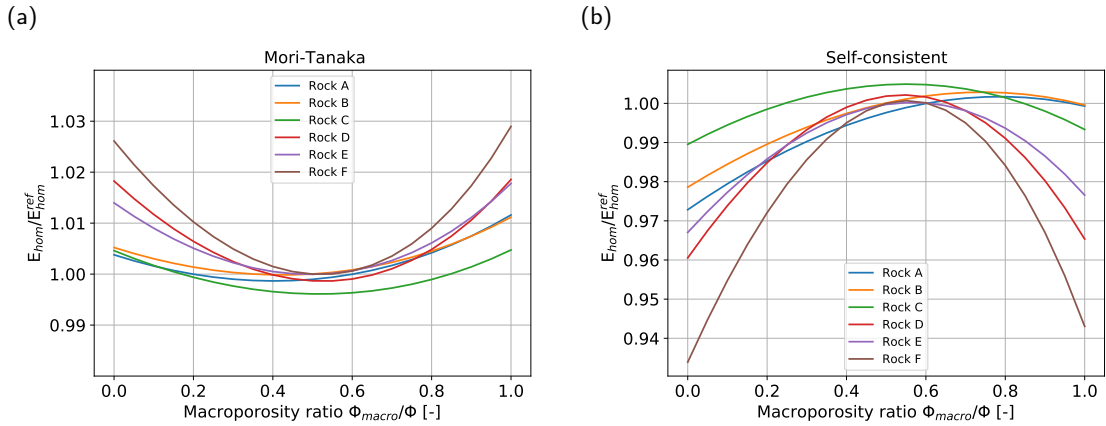


**Figure 15:** Relative errors linked to the distribution of porosity between macro and microporosity for **(a)** Mori-Tanaka and **(b)** self-consistent schemes.  $E_{hom}^{ref}$  stands for the homogenized Young's modulus obtained for the porosity diameter threshold set to 2  $\mu\text{m}$ .

Poisson's ratio of quartz is, in fact, equal to 0.08<sup>56</sup>. Still, the volume fraction of quartz is so low in all rocks considered (see Table 1) that the impact of the Poisson's ratio of quartz on the calculated homogenized modulus is negligible. To account for porosity, we introduce a phase with vanishing properties and a volume fraction equal to the global porosity given in Figure 1.

The ratios of the corresponding macroscopic homogenized Young's modulus to the experimental one are presented in Figure 14 for the six rocks. A mean overestimation factor of 1.62 is obtained with this approach, with a standard deviation of 0.24. The results indicate that the self-consistent indentation approach gives a very close estimation to that obtained with homogenization schemes applied after proper identification of the material's various mineralogical phases. Like those latter approaches, the self-consistent indentation approach can successfully predict if a rock is stiffer than another without requiring any direct characterization of the rock microstructure (but for the total porosity). This approach is convenient, although it provides less insight into the physical origin of the dispersion of Young's modulus. Anyhow, we found that the macroscopic elastic properties of the rocks are overestimated by homogenization, independent of whether homogenization is performed directly on the indentation grid (i.e., self-consistent indentation approach) or whether homogenization is performed after proper identification of the various mineralogical phases and their spatial organization.

## 5. Discussion and Exploratory Analyses

As seen in the previous section, the homogenized Young's moduli overestimate the measured ones. Many microstructural attributes can explain this result, such as:

- **The existence of cracks:** the media in the schemes are not considered fractured. However, cracks may exist in the phases, which would reduce the homogenized Young's modulus<sup>57,58</sup>.
- **The shape of the pores:** a spherical shape has been assumed for the phases in our homogenization procedure. However, the pore shapes observed in the SEM images are non-regular in most cases (e.g., Figures 6 and 7). For example, one can expect that pores' asphericity would reduce the predicted macroscopic Young's modulus<sup>59</sup>.
- **Interfaces behavior:** Perfect bonding among the phases is assumed in the homogenization models. This assumption is strong and may cause an overestimation of Young's modulus. One can expect that relaxing it (i.e., considering that there can be some discontinuity of displacements or stresses across an interface between phases) would reduce the estimated modulus<sup>60</sup>.

Introducing additional complexities translates into introducing additional parameters in the homogenization models. Despite being theoretically developed, the drawback of all these enhancements in homogenization is evaluating the introduced parameters from experimental methods. However, the impact of the first two factors listed above on homogenized Young's modulus is explored in the following subsections. Since the results of section 4 showed that the homogenization scheme had little impact on the homogenized results, this exploratory analysis is limited to one homogenization scheme, namely the Mori-Tanaka, which is computationally simpler than the self-consistent scheme.

### 5.1. Cracked Media

Expressions of the homogenized elastic moduli for a medium containing 3-D randomly oriented elliptic cracks have been developed and given by Pan and Weng<sup>59</sup>. A crack is assumed to have an ellipsoidal shape, with negligible thickness  $t$  and width  $w$  in comparison to the length  $l$ . Following Budiansky and O'connell<sup>61</sup>, a crack density parameter  $\eta$  is defined in terms of the crack properties as following:

$$\eta = \frac{2N}{\pi} \frac{A^2}{P} \quad (10)$$

where  $N$  represents the number of cracks per unit volume,  $A = \pi w l$  is the crack area, and  $P = 4l$  is its perimeter. The parameter  $\eta$  is somehow an indicator for the presence of cracks, as it increases when  $N$  becomes greater for uniform crack geometry or when cracks become larger for constant  $N$ . The expressions of the homogenized moduli in the case of a Mori-Tanaka scheme are given in terms of the elastic properties of the matrix and the parameter  $\eta$  as following:

$$K_{hom}^{\eta} = \frac{K_{mat}}{1 + \frac{16}{9} \frac{1-\nu_{mat}^2}{1-2\nu_{mat}} \eta} \quad (11)$$

$$G_{hom}^{\eta} = \frac{G_{mat}}{1 + \frac{8}{45} (10 - 7\nu_{mat}) \eta} \quad (12)$$

As a first qualitative approach, we consider elliptic cracks randomly oriented in the dominant phase of each rock at a lower scale (Scale 0 in Figures 13c and 13d). The ratios of the homogenized modulus to the macroscopic measured one are plotted for each rock in Figure 16. We observe that homogenization estimates the measured values for  $\eta$  ranging between 0.32 and 0.82. The results are consistent with the intensity of overestimation by the initial Mori-Tanaka model, i.e., the higher the overestimation, the greater the density parameter (see Figure 14). It is noticeable that  $\eta$  is the same for Rocks C and D (Facies F2) but exhibits a dispersion for rocks of Facies F1.



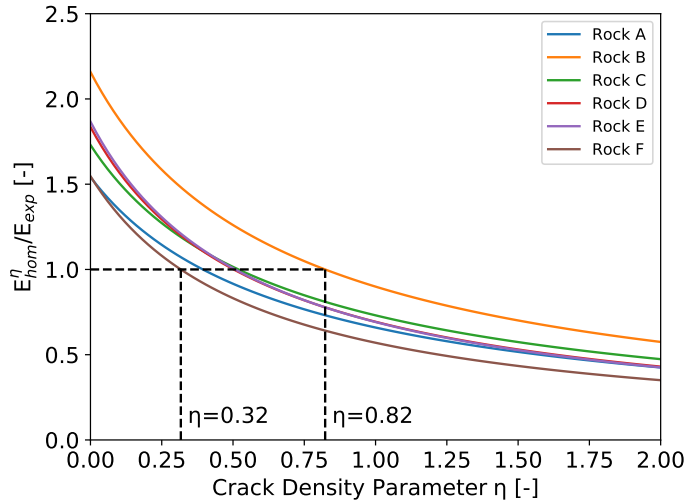


**Figure 16:** Homogenization results taking into account cracks in the dominant phase of each rock.

## 5.2. Spheroidal Pore Shapes

Pores are now assumed to have spheroidal shapes instead of spherical ones. This shape is illustrated in Figure 17a, where  $a_2 = a_3$  and the aspect ratio is defined as:

$$\alpha = \frac{a_1}{a_2} \quad (13)$$

Two cases can be distinguished depending on the value of this aspect ratio:

- The oblate shape for  $\alpha < 1$ .
- The prolate shape for  $\alpha > 1$ .

When the aspect ratio is equal to 1, the shape degenerates to a spherical one. The homogenization solution for a Mori-Tanaka scheme of a matrix containing 3-D randomly oriented spheroidal inclusions has been given by Tandon and Weng<sup>57</sup> and detailed later with examples in Zhao et al.<sup>62</sup> for the case of spheroidal pores. The expressions of the homogenized moduli are:

$$K_{hom}^{\alpha} = \frac{K_{mat}}{1 + \phi \cdot p} \quad (14)$$

$$G_{hom}^{\alpha} = \frac{G_{mat}}{1 + \phi \cdot q} \quad (15)$$

where  $\phi$  is the porosity,  $p$  and  $q$  are two expressions depending on the Eshelby tensor of a spheroidal inclusion. These expressions can be found in Zhao et al.<sup>62</sup> and in the shared Python script.

For the sake of simplicity, porosity is assumed to be completely present at Scale 1 of the schemes illustrated in Figures 13a and 13b (i.e.,  $\phi = \phi_{micro}$ ). It has been shown that the impact of such assumption is not significant on the homogenized moduli in the case of the Mori-Tanaka model (Figure 15). Equations 14 and 15 can thus be used and the ratios of homogenized over measured Young's modulus are plotted in Figure 17b. In agreement with the results published by Zhao et al.<sup>62</sup>, the stiffest medium is obtained in the case of spherical pores, which also corresponds to the upper bound of Hashin and Shtrikman<sup>57</sup>. In the case of oblate pores, the modulus rapidly decreases at a given porosity. However, considering prolate pores instead of spherical ones induces only a slight decrease in the material

stiffness. We observe that homogenization estimates Young's modulus's measured values for aspect ratios ranging from 0.033 to 0.103. As expected, the higher the initial overestimation factor (Figure 14), the lower the pore aspect ratio. However, the microstructures of the rocks inspected with SEM (Figures 6 to 8) indicate that the aspect ratio of the pores is much closer to one than those predicted by the inverse analysis performed here. Therefore, it would be interesting to consider more complex morphologies of pores, which consider an angular character (e.g., see Du et al.<sup>63</sup> for concave pores).

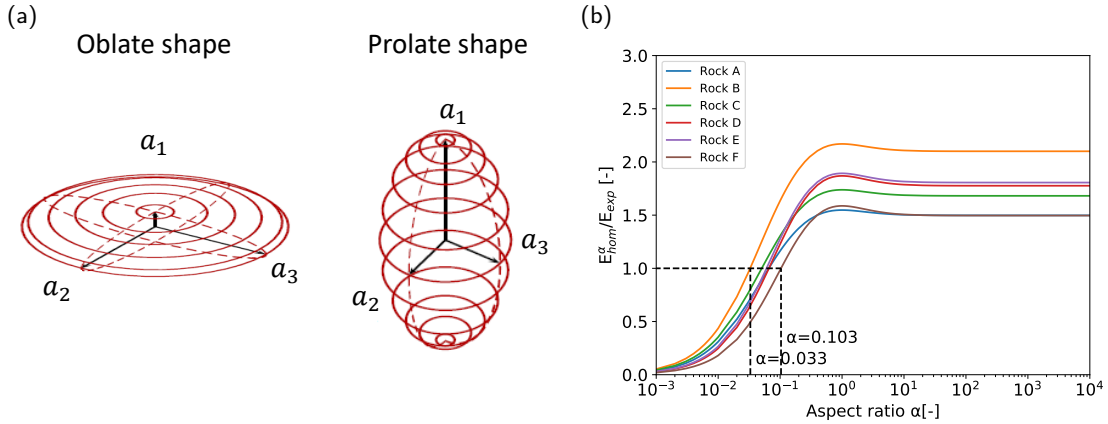


**Figure 17:** (a) Schematic of the spheroidal shape (from Barthelemy<sup>64</sup>); (b) Homogenization results taking into account randomly oriented spheroidal micropores ( $\phi = \phi_{micro}$ ).

### 5.3. Increasing the Studied Scale - Microindentation Tests

The nanoindentation tests of this study have been performed at a shallow penetration depth (200 nm), and the measured maximum force is around six mN (obtained while indenting the dolomite phase). These tests have been assumed to probe non-cracked solid subvolumes at a scale of around  $2 \mu\text{m}$ . To account for cracks and porosity, the probed subvolume must be enlarged by performing microindentation tests at higher levels of penetration depths (or equivalently force). If this subvolume becomes large enough to be statistically representative of the microstructure, we would expect to measure the macroscopic elastic properties of the rock directly from the microindentation tests. The existence of such subvolume is sought for Rocks A, B, and C through microindentation tests performed using a NHT<sup>3</sup> tester in the laboratory of Anton Paar GmbH up to 5 maximum force levels: 0.3 N, 1 N, 3 N, 10 N, and 30 N. For each loading level, ten tests are carried out in different zones chosen randomly on the surface of the polished samples. Therefore, 50 measurements are obtained for each sample.

The results are gathered with those of nanoindentation tests and are presented in Figure 18. Each point on the plots corresponds to the average value calculated over all the tests performed up to a loading level. The characteristic size of the probed volume is assumed to be ten times the maximum penetration depth. The results show a high dispersion, as the coefficient of variation of the microindentation Young's modulus and hardness can reach 20% and 45%, respectively (Figures 18c and 18d). In addition, these coefficients do not seem to decrease while increasing the characteristic size, which may be explained by the fact that the scale probed by the deepest microindentations is not sufficiently large compared to the scale of heterogeneity of microstructures (see Figure 5). Nonetheless, despite this dispersion, the plots of the mean value of indentation Young's modulus over macroscopic Young's modulus  $E_{exp}$  in Figures 18a and 18b show that while increasing the scale of the study, the indentation modulus becomes closer to the macroscopic value measured from triaxial experiments  $E_{exp}$ . However, the scale reached by microindentation is not sufficient to predict the macroscopic modulus. The convergence of Young's modulus of Rock B seems slower than that of Rocks A and C. This observation may be explained by the more pronounced microstructural heterogeneity of Rock B (see Section 3.1).

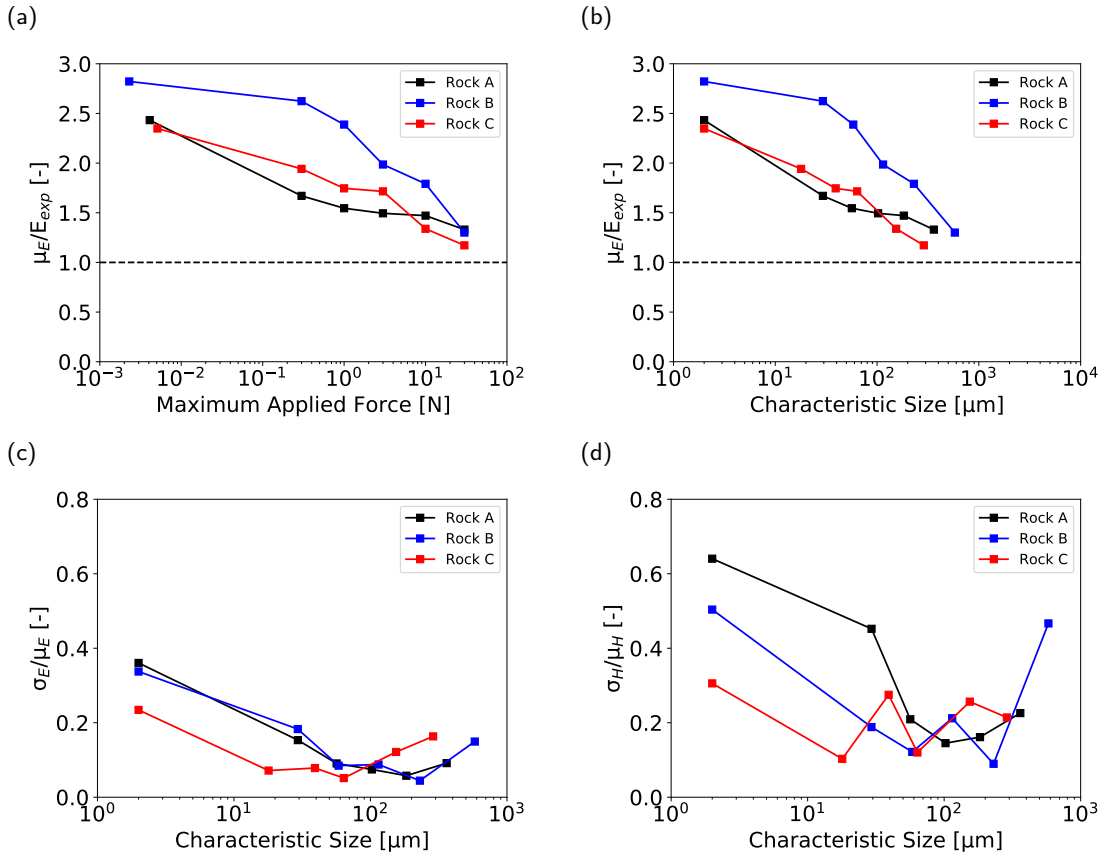


**Figure 18:** Microindentation and nanoindentation results obtained on Rocks A, B and C: Ratio of the mean indentation Young's modulus  $\mu_E$  over  $E_{exp}$  measured from macroscopic mechanical experiments plotted against (a) the maximum applied force; (b) the characteristic size of the probed volume. Coefficient of variation of the (c) indentation Young's modulus; (d) indentation hardness, with respect to the characteristic size of the probed volume.

## 6. Conclusions

From a methodological point of view, we have shown that the nanoindentation technique can be applied to carbonate rocks with a wide range of porosities and microstructures. In conjunction with SEM-EDS analyses, we have also shown that nanoindentation could yield valuable information regarding the mechanical properties of the rock's phases. This piece of information made it possible to shed light on the microscopic origin of the dispersion of macroscopic elastic properties. As a perspective, nanoindentation combined with SEM-EDS analysis can be applied, beyond carbonate rocks, to a wide range of heterogeneous materials. Besides, the main conclusions of this study are listed in the following:

1. A full experimental program is developed to couple the indentation measurements and SEM-EDS mapping. The protocol is enriched to solve several issues that the experimenter encounters and provide all the inputs required for homogenization.
2. The mineral composition and mechanical properties of carbonate rocks are main microstructural features controlling the macroscopic elastic properties. Two rocks having the same global porosity can have different proportions of mineral phases and/or different mineral mechanical properties, leading to a significant variation of their macroscopic elastic properties. Dolomite is found to be harder and stiffer than calcite, and a presence of such a phase would reinforce carbonate rocks.
3. The homogenization theory is applied in this study to predict the macroscopic Young's moduli of the rocks. Results show that this technique applied on data obtained at the submicron scale can successfully capture

the macroscopic Young's modulus trend in the sense that it can indicate if a rock is more or less stiff than another one. However, an overestimation of a factor around  $1.78 \pm 0.23$  (in Mori-Tanaka case) and  $1.72 \pm 0.24$  (in self-consistent case) is systematically obtained between the homogenized and measured macroscopic ones.

4. Homogenization through self-consistent indentation approach proposed by Randall et al.<sup>55</sup> is found to give very close results to those obtained through upscaling schemes fed with the procedure combining nanoindentation and SEM-EDS imaging, and identifying the various mineralogical phases, their volume fractions, mechanical properties, and spatial organization. The former approach is quicker, simpler, and can predict if a rock is stiffer than another. However, the combined nanoindentation and SEM-EDS imaging approach, although more complex, provides greater insight into the physical origin of the dispersion of the macroscopic Young's modulus.
5. Some microstructural features that can explain the macroscopic Young's modulus overestimation are listed, and two of them are investigated: the presence of cracks and the non-spherical shape of pores. Accounting for cracks with a crack density parameter between 0.32 and 0.82 is required to predict a macroscopic Young's modulus of carbonate rocks consistent with the measured ones. However, it is difficult to measure this parameter directly from image analysis. As for the pore geometry feature, spheroidal pores with aspect ratios ranging from 0.033 and 0.104 randomly oriented in the space permit the prediction of the measured macroscopic modulus. However, these aspect ratios do not seem realistic, as the observed pores in the SEM images suggest that the pores are much less aspherical than back-calculated from modeling.
6. The scale of study has been enlarged through microindentation tests. Although the indentation elastic modulus becomes closer to the macroscopic value when the indentation depth increases, microindentation does not seem to reach a scale sufficiently large to make it possible to measure the macroscopic Young's modulus of carbonate rocks directly.

## A. Geometric Transformation to Find the Positions of the Indentation Imprints

The indentation grids no longer have a regular square shape in the SEM images. Thus, a geometric transformation of the square to a random quadrangle is proposed based on the corners' positions. A schematic illustration is given in Figure 19.

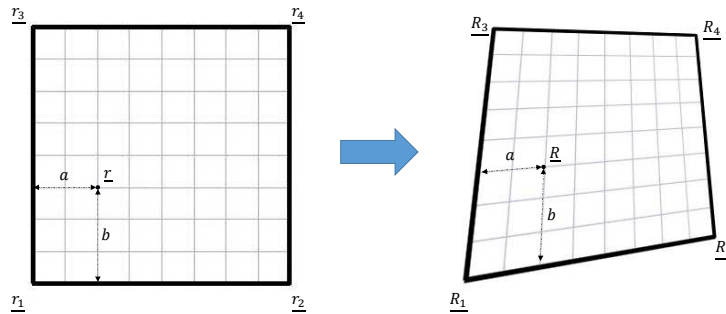


**Figure 19:** Schematic of the considered geometric transformation to calculate the positions of all the imprints of a grid.

Let  $(\underline{r}_i)_{i=1,2,3,4}$  and  $(\underline{R}_i)_{i=1,2,3,4}$  denote the position vectors of the four corners before and after the transformation, respectively. Let  $\underline{r}$  and  $\underline{R}$  denote the position vectors of an intermediate point (or an imprint in our case) before and after the transformation, respectively. In the initial configuration,  $\underline{r}$  can be expressed in terms of the coordinates of the four corners as:

$$\begin{aligned} \underline{r} = \underline{r}_1 &+ a \left[ (1-b)(\underline{r}_2 - \underline{r}_1) + \frac{b}{2}(\underline{r}_4 - \underline{r}_1) \right] \\ &+ b \left[ (1-a)(\underline{r}_3 - \underline{r}_1) + \frac{a}{2}(\underline{r}_4 - \underline{r}_1) \right] \end{aligned} \quad (16)$$

where the parameters  $a$  and  $b$  vary between 0 and 1. When these parameters take simultaneously the values of 0 and/or 1, the position vector is nothing else than that of one of the corners. Likewise, the coordinates of the same

point in the deformed configuration can be expressed using the same values for  $a$  and  $b$ , such as:

$$\underline{R} = \underline{R}_1 + a \left[ (1-b)(\underline{R}_2 - \underline{R}_1) + \frac{b}{2}(\underline{R}_4 - \underline{R}_1) \right] + b \left[ (1-a)(\underline{R}_3 - \underline{R}_1) + \frac{a}{2}(\underline{R}_4 - \underline{R}_1) \right] \quad (17)$$

Since the position vectors of the 4 corners are known in both configurations, the evaluation of  $a$  and  $b$  can be done using Equation 16 and the identification of the vector position  $\underline{R}$  is straightforward using Equation 17.

## Acknowledgment

This work was carried out with funding from Total (now TotalEnergies SE). We thank Pierre Barlet from TotalEnergies SE for the triaxial tests.

## Conflict of Interest

The authors declare that there are no known conflicts of interest associated with this publication.

## Code Availability

Python scripts relative to the current article are available for interested readers at the following link: <https://doi.org/10.5281/zenodo.4452014>.

## References

1. Wilkinson BH, McElroy BJ, Kesler SE, Peters SE, Rothman ED. Global geologic maps are tectonic speedometers - Rates of rock cycling from area-age frequencies. *Geological Society of America Bulletin* 2009;121(5-6):760–779. doi:10.1130/B26457.1.
2. Tester JW, Anderson BJ, Batchelor A, Blackwell D, DiPippo R, Drake E, Garnish J, Livesay B, Moore M, Nichols K, et al. The future of geothermal energy. *Massachusetts Institute of Technology* 2006;358.
3. Rutqvist J. The geomechanics of CO<sub>2</sub> storage in deep sedimentary formations. *Geotechnical and Geological Engineering* 2012;30(3):525–551. doi:10.1007/s10706-011-9491-0.
4. Choquette PW, Pray LC. Geologic nomenclature and classification of porosity in sedimentary carbonates. *AAPG bulletin* 1970;54(2):207–250. doi:10.1306/5D25C98B-16C1-11D7-8645000102C1865D.
5. Eberli GP, Baechle GT, Anselmetti FS, Incze ML. Factors controlling elastic properties in carbonate sediments and rocks. *The Leading Edge* 2003;22(7):654–660. doi:10.1190/1.1599691.
6. Flügel E. Microfacies of carbonate rocks: analysis, interpretation and application. Berlin: Springer Science & Business Media; 2004.
7. Weger RJ, Eberli GP, Baechle GT, Massaferro JL, Sun YF. Quantification of pore structure and its effect on sonic velocity and permeability in carbonates. *AAPG bulletin* 2009;93(10):1297–1317. doi:10.1306/05270909001.
8. Fournier F, Leonide P, Biscarrat K, Gallois A, Borgomano J, Foubert A. Elastic properties of microporous cemented grainstones. *Geophysics* 2011;76(6):E211–E226. doi:10.1190/geo2011-0047.1.
9. Kalo K, Grgic D, Auvray C, Giraud A, Drach B, Sevostianov I. Effective elastic moduli of a heterogeneous oolitic rock containing 3-D irregularly shaped pores. *International Journal of Rock Mechanics and Mining Sciences* 2017;98:20–32. doi:10.1016/j.ijrmmms.2017.07.009.
10. Ulm FJ, Vandamme M, Bobko C, Alberto Ortega J, Tai K, Ortiz C. Statistical indentation techniques for hydrated nanocomposites: concrete, bone, and shale. *Journal of the American Ceramic Society* 2007;90(9):2677–2692. doi:10.1111/j.1551-2916.2007.02012.x.
11. Ma Z, Gamage RP, Zhang C. Application of nanoindentation technology in rocks: a review. *Geomechanics and Geophysics for Geo-Energy and Geo-Resources* 2020;6(4):1–27. doi:10.1007/s40948-020-00178-6.
12. Vialle S, Lebedev M. Heterogeneities in the elastic properties of microporous carbonate rocks at the microscale from nanoindentation tests. In: *SEG Technical Program Expanded Abstracts 2015*. Society of Exploration Geophysicists; 2015:3279–3284.
13. Zhang Y, Lebedev M, Al-Yaseri A, Yu H, Nwidee LN, Sarmadivaleh M, Barifcani A, Iglauder S. Morphological evaluation of heterogeneous oolitic limestone under pressure and fluid flow using X-ray microtomography. *Journal of Applied Geophysics* 2018;150:172–181. doi:10.1016/j.jappgeo.2018.01.026.
14. Lebedev M, Wilson ME, Mikhaltsevitch V. An experimental study of solid matrix weakening in water-saturated Savonnières limestone: Solid matrix weakening in water-saturated limestone. *Geophysical Prospecting* 2014;62(6):1253–1265. doi:10.1111/1365-2478.12168.
15. Lebedev M, Zhang Y, Sarmadivaleh M, Barifcani A, Al-Khdheawi E, Iglauder S. Carbon geosequestration in limestone: Pore-scale dissolution and geomechanical weakening. *International Journal of Greenhouse Gas Control* 2017;66:106–119. doi:10.1016/j.ijggc.2017.09.016.

16. Zhang Y, Lebedev M, Sarmadivaleh M, Barifcani A, Iglaier S. Change in geomechanical properties of limestone due to supercritical CO<sub>2</sub> injection. In: *SPE Asia Pacific Oil & Gas Conference and Exhibition*. OnePetro; 2016:.
17. Vialle S, Pazdniakou A, Adler P, et al. Prediction of the macroscopic mechanical properties of carbonate from nano-indentation tests. In: *52nd US Rock Mechanics/Geomechanics Symposium*. American Rock Mechanics Association; 2018:.
18. Doube M, Firth EC, Boyde A, Bushby AJ. Combined nanoindentation testing and scanning electron microscopy of bone and articular calcified cartilage in an equine fracture predilection site. *European cells materials* 2010;19:242–51. doi:10.22203/ecm.v019a23.
19. Yang C, Xiong Y, Wang J, Li Y, Jiang W. Mechanical characterization of shale matrix minerals using phase-positioned nanoindentation and nano-dynamic mechanical analysis. *International Journal of Coal Geology* 2020;229:103571. doi:10.1016/j.coal.2020.103571.
20. Liu Y, Liu A, Liu S, Kang Y. Nano-scale mechanical properties of constituent minerals in shales investigated by combined nanoindentation statistical analyses and sem-edx-rd techniques. *International Journal of Rock Mechanics and Mining Sciences* 2022;159:105187. doi:10.1016/j.ijrmmms.2022.105187.
21. Abedi S, Slim M, Hofmann R, Bryndzia T, Ulm FJ. Nanochemo-mechanical signature of organic-rich shales: a coupled indentation–edx analysis. *Acta Geotechnica* 2016;11(3):559–572. doi:10.1007/s11440-015-0426-4.
22. Mashhadani M, Verde A, Sharma P, Abedi S. Assessing mechanical properties of organic matter in shales: Results from coupled nanoindentation/sem-edx and micromechanical modeling. *Journal of Petroleum Science and Engineering* 2018;165:313–324. doi:10.1016/j.petro.2018.02.039.
23. Veytskin YB, Tammina VK, Bobko CP, Hartley PG, Clennell MB, Dewhurst DN, Dagastine RR. Micromechanical characterization of shales through nanoindentation and energy dispersive x-ray spectrometry. *Geomechanics for Energy and the Environment* 2017;9:21–35. doi:https://doi.org/10.1016/j.gete.2016.10.004.
24. Kumar V, Sondergeld CH, Rai CS. Nano to Macro Mechanical Characterization of Shale. SPE Annual Technical Conference and Exhibition; 2012:doi:10.2118/159804-MS.
25. Mason J, Carloni J, Zehnder A, Baker SP, Jordan T. Dependence of Micro-Mechanical Properties on Lithofacies: Indentation Experiments on Marcellus Shale. SPE/AAPG/SEG Unconventional Resources Technology Conference; 2014:doi:10.15530/URTEC-2014-1922919; uRTEC-1922919-MS.
26. Chen JJ, Sorelli L, Vandamme M, Ulm FJ, Chanvillard G. A coupled nanoindentation/sem-edx study on low water/cement ratio portland cement paste: evidence for c–s–h/ca (oh) 2 nanocomposites. *Journal of the American Ceramic Society* 2010;93(5):1484–1493. doi:10.1111/j.1551-2916.2009.03599.x.
27. Wilson W, Rivera-Torres J, Sorelli L, Durán-Herrera A, Tagnit-Hamou A. The micromechanical signature of high-volume natural pozzolan concrete by combined statistical nanoindentation and sem-edx analyses. *Cement and Concrete Research* 2017;91:1–12. doi:https://doi.org/10.1016/j.cemconres.2016.10.004.
28. Moser RD, Allison PG, Chandler MQ. Characterization of impact damage in ultra-high performance concrete using spatially correlated nanoindentation/sem-edx. *Journal of Materials Engineering and Performance* 2013;22(12):3902–3908. doi:10.1007/s11665-013-0668-y.
29. Zhang Y, Liang M, Gan Y, Çopuroğlu O. Micro-mechanical properties of slag rim formed in cement-slag system evaluated by nanoindentation combined with sem. *Materials* 2022;15(18). doi:10.3390/ma15186347.
30. Sorelli L, Pham DT, Vallée D, Chen J, Fafard M. Finite Element Based Characterization of the Creep Properties of the Cement Paste Phases by Coupling Nanoindentation Technique and SEM-EDS. 2013:182–189. doi:10.1061/9780784413111.021.
31. Bu Y, Saldana C, Handwerker C, Weiss J. The Role of Calcium Hydroxide in the Elastic and Viscoelastic Response of Cementitious Materials: A Nanoindentation and SEM-EDS Study. In: Sobolev K, Shah SP, eds. *Nanotechnology in Construction*. Cham: Springer International Publishing. ISBN 978-3-319-17088-6; 2015:25–34.
32. Deirieh A, Ortega JA, Ulm FJ, Abousleiman Y. Nanochemomechanical assessment of shale: a coupled WDS-indentation analysis. *Acta Geotechnica* 2012;7(4):271–295. doi:10.1007/s11440-012-0185-4.
33. Krakowiak KJ, Wilson W, James S, Musso S, Ulm FJ. Inference of the phase-to-mechanical property link via coupled X-ray spectrometry and indentation analysis: Application to cement-based materials. *Cement and Concrete Research* 2015;67:271–285. doi:10.1016/j.cemconres.2014.09.001.
34. Cała M, Cyran K, Kawa M, Kolano M, Łydźba D, Pachnicz M, Rajczakowska M, Rózański A, Sobótka M, Stefaniuk D, et al. Identification of microstructural properties of shale by combined use of X-ray micro-CT and nanoindentation tests. *Procedia engineering* 2017;191:735–743. doi:10.1016/j.proeng.2017.05.239.
35. Ahmadvor R, Vanorio T, Mavko G. Confocal laser scanning and atomic-force microscopy in estimation of elastic properties of the organic-rich bazhenov formation. *The Leading Edge* 2009;28(1):18–23. doi:10.1190/1.3064141.
36. Shukla P, Kumar V, Curtis M, Sondergeld CH, Rai CS, et al. Nanoindentation studies on shales. In: *47th US Rock Mechanics/Geomechanics Symposium*. American Rock Mechanics Association; 2013:.
37. Constantinides G, Chandran KR, Ulm FJ, Van Vliet K. Grid indentation analysis of composite microstructure and mechanics: Principles and validation. *Materials Science and Engineering: A* 2006;430(1-2):189–202. doi:10.1016/j.msea.2006.05.125.
38. Lura P, Triuk P, Münch B. Validity of recent approaches for statistical nanoindentation of cement pastes. *Cement and Concrete Composites* 2011;33(4):457–465. doi:10.1016/j.cemconcomp.2011.01.006.
39. Tazi H. Propriétés élastiques et anisotropie des roches mères : approche expérimentale multi-échelle et modélisation par milieu effectif. PhD dissertation; Université Paris-Est; 2019. URL: <https://pastel.archives-ouvertes.fr/tel-02878713>.
40. Rugar D, Hansma P. Atomic force microscopy. *Physics today* 1990;43(10):23–30.
41. Nguyen DL. Nouvelle méthodologie d'identification des propriétés mécaniques locales d'un matériau hétérogène par nanoindentation - application aux matériaux du génie civil. PhD dissertation; Université Paris-Est; 2017. URL: <https://pastel.archives-ouvertes.fr/tel-01730567>.



42. Miller M, Bobko C, Vandamme M, Ulm FJ. Surface roughness criteria for cement paste nanoindentation. *Cement and Concrete Research* 2008;38(4):467–476. doi:10.1016/j.cemconres.2007.11.014.
43. Donnelly E, Baker SP, Boskey AL, van der Meulen MC. Effects of surface roughness and maximum load on the mechanical properties of cancellous bone measured by nanoindentation. *Journal of Biomedical Materials Research Part A: An Official Journal of The Society for Biomaterials, The Japanese Society for Biomaterials, and The Australian Society for Biomaterials and the Korean Society for Biomaterials* 2006;77(2):426–435. doi:10.1002/jbm.a.30633.
44. VanLandingham MR. Review of instrumented indentation. *Journal of Research of the National Institute of Standards and Technology* 2003;108(4):249. doi:10.6028/jres.108.024.
45. Larson P, Giannakopoulos A, Söderlund E, Rowcliffe D, Vestergaard R. Analysis of berkovich indentations. *Int J Solids Struct* 1996;33:221–248. doi:10.1016/0020-7683(95)00033-7.
46. Oliver WC, Pharr GM. An improved technique for determining hardness and elastic modulus using load and displacement sensing indentation experiments. *Journal of materials research* 1992;7(6):1564–1583. doi:10.1557/JMR.1992.1564.
47. Tabor D. The hardness of metals. Oxford university press; 2000.
48. Ganneau F, Constantinides G, Ulm FJ. Dual-indentation technique for the assessment of strength properties of cohesive-frictional materials. *International journal of solids and structures* 2006;43(6):1727–1745. doi:10.1016/j.ijsolstr.2005.03.035.
49. Fialips CI, Labeyrie B, Burg V, Mazière V, Munerel Y, Haurie H, Jolivet I, Lasnel R, Laurent JP, Lambert L, Jacquelin-Vallée L. Quantitative Mineralogy of Vaca Muerta and Alum Shales From Core Chips and Drill Cuttings by Calibrated SEM-EDS Mineralogical Mapping. In: *Proceedings of the 6th Unconventional Resources Technology Conference*. Houston, Texas, USA: American Association of Petroleum Geologists. ISBN 978-0-9912144-5-7; 2018;doi:10.15530/urtec-2018-2902304.
50. Delesse M. Procédé mécanique pour déterminer la composition des roches. *CR Acad Sci Paris* 1847;25:544–545.
51. Zaoui A. Matériaux hétérogènes et composites: majeure de mécanique, option matériaux et structures: promotion 1998, majeure 1, 2e année. École polytechnique; 2000.
52. Eshelby JD. The determination of the elastic field of an ellipsoidal inclusion, and related problems. *Proceedings of the royal society of London Series A Mathematical and physical sciences* 1957;241(1226):376–396.
53. Mori T, Tanaka K. Average stress in matrix and average elastic energy of materials with misfitting inclusions. *Acta metallurgica* 1973;21(5):571–574. doi:10.1016/0001-6160(73)90064-3.
54. Hershey A. The elasticity of an isotropic aggregate of anisotropic cubic crystals. *Journal of Applied mechanics-transactions of the ASME* 1954;21(3):236–240.
55. Randall NX, Vandamme M, Ulm FJ. Nanoindentation analysis as a two-dimensional tool for mapping the mechanical properties of complex surfaces. *Journal of materials research* 2009;24(3):679–690. doi:10.1557/jmr.2009.0149.
56. Gercek H. Poisson's ratio values for rocks. *International Journal of Rock Mechanics and Mining Sciences* 2007;44(1):1–13. doi:10.1016/j.ijrmms.2006.04.011.
57. Tandon G, Weng G. Average stress in the matrix and effective moduli of randomly oriented composites. *Composites science and technology* 1986;27(2):111–132. doi:10.1016/0266-3538(86)90067-9.
58. Dormieux L, Kondo D, Ulm FJ. Microporomechanics. John Wiley & Sons; 2006.
59. Pan H, Weng G. Elastic moduli of heterogeneous solids with ellipsoidal inclusions and elliptic cracks. *Acta mechanica* 1995;110(1-4):73–94. doi:10.1007/BF01215417.
60. Ghabezloo S. A micromechanical model for the effective compressibility of sandstones. *European Journal of Mechanics-A/Solids* 2015;51:140–153. doi:10.1016/j.euromechsol.2014.12.007.
61. Budiansky B, O'connell RJ. Elastic moduli of a cracked solid. *International journal of Solids and structures* 1976;12(2):81–97. doi:10.1016/0020-7683(76)90044-5.
62. Zhao Y, Tandon G, Weng G. Elastic moduli for a class of porous materials. *Acta Mechanica* 1989;76(1-2):105–131. doi:10.1007/BF01175799.
63. Du K, Cheng L, Barthélémy JF, Sevostianov I, Giraud A, Adessina A. Effective elastic properties of transversely isotropic materials with concave pores. *Mechanics of Materials* 2021;153:103665. doi:10.1016/j.mechmat.2020.103665.
64. Barthelemy JF. Approche micromécanique de la rupture et de la fissuration dans les géomatériaux. Ph.D. thesis; Ecole des Ponts ParisTech; 2005.